tds00 | ACSJCA | JCA10.0.1465/W Unicode | research.3f (R3.6.i11:4432 | 2.0 alpha 39) 2015/07/15 14:30:00 | PROD-JCA1 | rq_6261726 | 10/10/2016 08:38:02 | 19 | JCA-DEFAULT

CHEMISTRY OF MATERIALS

Article

pubs.acs.org/cm

# $La_3Li_3W_2O_{12}$: Ionic Diffusion in a Perovskite with Lithium on both A- and B-Sites

Alma B. Santibáñez-Mendieta,[†] Christophe Didier,[†] Kenneth K. Inglis,[†] Alex J. Corkett,[†] Michael J. Pitcher,[†] Marco Zanella,[†] J. Felix Shin,[†] Luke M. Daniels,[†] Aydar Rakhmatullin,[‡] Ming Li,[§] Matthew S. Dyer,[†] John B. Claridge,[†] Frédéric Blanc,[*,†,∥] and Matthew J. Rosseinsky[*,†]

[†]Department of Chemistry, University of Liverpool, Crown Street, Liverpool L69 7ZD, United Kingdom

[‡]CEMHTI-CNRS UPR3079, Conditions Extrêmes et Matériaux: Haute Température et Irradiation, Av. de la Recherche Scientifique, 45071 Orléans cedex 2, France

[§]Faculty of Engineering, University of Nottingham, University Park, Nottingham NG7 2RD, United Kingdom

[∥]Stephenson Institute for Renewable Energy, University of Liverpool, Crown Street, Liverpool L69 7ZD, United Kingdom

*Supporting Information*

**ABSTRACT:** The structure and $Li^+$ ion dynamics of a new class of $ABO_3$ perovskite with Li on both the A- and B-sites are described. $La_3Li_3W_2O_{12}$ is synthesized by solid state reaction at 900 °C and shown by powder X-ray diffraction to adopt the structure of a monoclinic double perovskite $(A_2)BB'O_6$, $(La_{1.5}Li_{0.5})WLiO_6$, with rock salt order of $W^{6+}$ and $Li^+$ on the B-site. High resolution powder neutron diffraction locates A-site Li in a distorted tetrahedron displaced from the conventional perovskite A-site, which differs considerably from the sites occupied by Li in the well studied $La_{2/3-x}Li_{3x}TiO_3$ family. This is confirmed by the observation of a lower coordinated $Li^+$ ion in the $^6Li$ magic angle spinning nuclear magnetic resonance (NMR) spectra, in addition to the B-site $LiO_6$, and supported computationally by density functional theory (DFT), which also suggests local order of A-site $La^{3+}$ and $Li^+$. DFT shows that the vacancies necessary for transport can arise from Frenkel or La excess defects, with an energetic cost of ~0.4 eV/vacancy in both cases. *Ab initio* molecular dynamics establishes that the $Li^+$ ion dynamics occur by a pathway involving a series of multiple localized Li hops between two neighboring A-sites with an overall energy barrier of ~0.25 eV, with additional possible pathways involving Li exchange between the A- and B-sites. A similar activation energy for $Li^+$ ion mobility (~0.3 eV) was obtained from variable temperature $^6Li$ and $^7Li$ line narrowing and relaxometry NMR experiments, suggesting that the barrier to Li hopping between sites in $La_3Li_3W_2O_{12}$ is comparable to the best oxide $Li^+$ ion conductors. AC impedance-derived conductivities confirm that $Li^+$ ions are mobile but that the long-range $Li^+$ diffusion has a higher barrier (~0.5 eV) which may be associated with blocking of transport by A-site $La^{3+}$ ions.

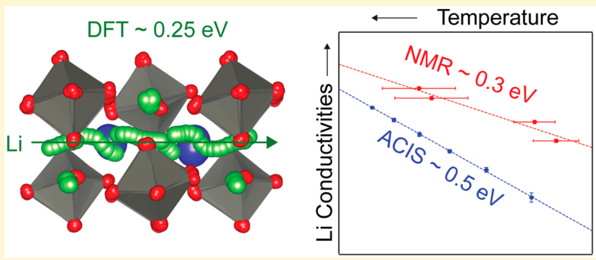


## 1. INTRODUCTION

Replacing liquid electrolytes with solid ceramics or polymers in next-generation battery technologies is of growing interest due to the major impact that will result from the increase in lifetime and safety, higher power outputs and higher energy densities expected in energy storage appliances.[1] Lithium has become the element of choice in most battery designs because of the high mobilities arising from its small ionic radius. Hence, a major goal of the field is to synthesize lithium-based ceramics with ionic conductivities that equal or surpass current liquid electrolytes.

The fastest crystalline inorganic $Li^+$ ion conductors reported to date are sulfides such as $Li_{10}GeP_2S_{12}$,[2] with a room temperature conductivity of 0.012 S/cm and the related $Li_{11}Si_2PS_{12}$.[3] The high conductivities arise from the presence of many potential sites for the Li cations that provide low energy pathways through these structures. Despite their high $Li^+$ conductivities, the practical applications of these compounds are limited by their tendency to decompose under ambient conditions, producing $H_2S$ when in contact with moisture, which necessitates handling in inert atmospheres.[4] Oxides are generally more chemically stable, and the doped garnet $Li_7La_3Zr_2O_{12}$ and the $ABO_3$ perovskite $La_{2/3-x}Li_{3x}TiO_3$ (LLTO; A = La, Li, B = Ti) systems have respectable conductivities in the region of $10^{-3}$ S/cm which arise from motion of the Li occupying the A-site between the $O_{12}$ anion cages that define these sites.[5,6] However, bulk ionic conductivity in LLTO may be limited by the presence of $La^{3+}$ rich and $La^{3+}$ poor A-site layers within the crystal structure, arising from the 2D diffusion of $Li^+$ ions at lower temperature and 3D diffusion at higher temperature.[7−9] In addition, the grain boundary conductivity is 1 order of magnitude lower than

Received: August 9, 2016
Revised: September 28, 2016





DOI: 10.1021/acs.chemmater.6b03220
*Chem. Mater.* XXXX, XXX, XXX−XXX

the bulk conductivity, reducing the total conductivity of LLTO ceramics,[5] and the reduction of $Ti^{4+}$ to $Ti^{3+}$ at the anode side of a cell leads to electronic conductivity and limits the practical use of LLTO as a $Li^+$ ion electrolyte.[10] One solution to the problem of high electronic contribution to the conductivity is to replace $Ti^{4+}$ with stable $4d^0$ or $5d^0$ cations such as $Nb^{5+}$ and $W^{6+}$: this has inspired the synthesis of several analogues of LLTO, including the perovskites $La_{1/3-x}Li_{3x}NbO_3$ ($x < 0.1$),[11,12] $La_{1/3-x}Li_{3x}TaO_3$[13−16] ($x < 0.17$) and the double perovskite $La_{4-x}Li_{3x}Mg_3W_3O_{18}$[17] ($x < 0.05$) in which $Li^+$ ions have been introduced to the partially vacant A-site by aliovalent substitution. The activation energies for Li conduction in such compounds are thought to be affected by the size of the windows between A-sites (dependent on the size of the B cation and directly affected by structural distortion), and also by the degree of covalency in the B−O bond,[17] as implied by the complex variation of ionic conductivity with composition and lattice parameter in LLTO-derived systems such as $(La_{1-x}Nd_x)_{0.56}Li_{0.33}Ti_{1-x}O_3$ and $La_{0.56}Li_{0.33}M_xTi_{1-x}O_3$ (M = $Zr^{4+}$, $Hf^{4+}$),[18,19] and related double perovskite systems such as $LiSr_{2-x}Ti_{2-2x}Ta_{1+2x}O_9$,[20,21] whose octahedral $BO_6$ networks are not distorted substantially away from those of LLTO. Despite the suppression of electronic conductivity in these compounds, the resulting ionic conductivities are lower than those seen in LLTO.

One approach to increasing ionic conductivity is to increase the number of potential migration pathways for $Li^+$ ions. The perovskite A-site is not the only position that can accommodate $Li^+$ ions; there are many known double perovskites in which the B-site is occupied by an ordered array of $Li^+$ ions and a tetra-, penta- or hexavalent cation, such as $LaLi_{1/3}Ti_{2/3}O_3$ (which exists in the same $La_2O_3-Li_2O-TiO_2$ phase diagram as LLTO[22,23]), $SrLi_{0.4}W_{0.6}O_3$[24] and the series $La_2LiMO_6$ (M = V, Nb, Ta, Mo, Re, Ru, Os, Ir and Sb),[25−27] as well as perovskites with combinations of Li, Nb and W on the B-site.[28,29] Such compounds retain the advantage of negligible electronic conductivity, but are rarely considered as ionic conductors due to the lack of an obvious conduction pathway between Li sites, and the paucity of examples of stable B-site vacancies in perovskites. However, consideration of intersite distances in the perovskite structure suggests that their structural features may offer a way of enhancing the ionic conductivities of the A-site Li perovskites: assuming an undistorted double perovskite with 1:1 rock-salt ordering on the B-sites, the distance between adjacent B- and A-sites (= $\sqrt{3/2}a_p$) is considerably shorter than that between two B-site $Li^+$ ions ($\sqrt{2}a_p$) and shorter than that between two adjacent A-sites ($a_p$). Hence, it is plausible that a perovskite with Li on both the A- and B-sites would exhibit exchange between the sites, offering the potential to enhance ionic conductivity considerably by opening up multiple pathways to $Li^+$ ion motion throughout the crystal structure. To date, there have been no reports of such a compound, despite the prevalence of both individual classes of structure.

Here we present the synthesis of such a material with composition $La_3Li_3W_2O_{12}$, in which one-quarter of the A-sites and one-half of the B-sites are occupied by $Li^+$ ions. The composition, crystal structure and $Li^+$ ion dynamics of $La_3Li_3W_2O_{12}$ are obtained and discussed through a combination of experimental and computational techniques. X-ray and neutron diffraction, electron microscopy and solid-state $^6$Li nuclear magnetic resonance (NMR) spectroscopy experiments combined with density functional theory (DFT) calculations are used to provide understanding of the crystal structure and the local Li environments. Additionally, insights into the $Li^+$ ion dynamics are obtained by acquiring variable temperature $^6$Li and $^7$Li solid-state NMR data and measuring the $Li^+$ ion conductivities by AC impedance spectroscopy (ACIS), and supported by computational modeling using *ab initio* molecular dynamics (AIMD) simulations.

## 2. MATERIALS AND METHODS

**2.1. Synthesis and Chemical Analysis.** *$La_3Li_3W_2O_{12}$*. Powder samples of $La_3Li_3W_2O_{12}$ were prepared by a conventional high-temperature ceramic method. A stoichiometric mixture of $La_2O_3$ (99.99% Sigma-Aldrich, dried at 950 °C for 12 h), $Li_2CO_3$ (>99% Sigma-Aldrich, dried at 250 °C for 12 h) and $WO_3$ (99.9% Fluka, dried at 250 °C for 12 h) was ball-milled in ethanol; the resulting slurry was then dried, homogenized with a pestle and mortar (thus reversing any possible separation of the reactants by sedimentation upon drying), and a portion of the reaction mixture was pelletized. The pellet was loaded into an alumina crucible lined with gold foil, buried in sacrificial powder of the same composition (i.e., the remainder of the reaction mixture), and subjected to a two-step firing process: first, the sample was heated in air to 900 °C at a rate of 5 °C/min and held for 5 h before cooling back to room temperature at 5 °C/min. PXRD shows that this step produces the targeted perovskite phase, but its crystallinity is relatively low, as indicated by broad Bragg peaks. To improve the crystallinity and homogeneity, the sample was reground by hand, repelletized, loaded into a gold-foil-lined alumina crucible and packed under the same sacrificial powder, and then subjected to a second annealing in air at 900 °C for 60 h (heated and cooled at a rate of 5 °C/min). This was found to produce highly crystalline single-phase samples of $La_3Li_3W_2O_{12}$.

*$La_{2/3}Li_{0.4}W_{0.6}O_3$*. For the initial synthesis of samples purified with washing, a mixture of $La_2O_3$ (99.99% Sigma-Aldrich, dried at 900 °C overnight), $Li_2CO_3$ (>99% Sigma-Aldrich, dried at 250 °C overnight) and $WO_3$ (99.9% Fluka, dried at 250 °C overnight) for target composition $La_{2/3}Li_{1.34}W_{0.6}O_{3.3}$ was ball-milled overnight, and pelletized after homogenization in a mortar. A gold foil was placed between the alumina crucible and the pellet itself was covered in sacrificial powder of the same composition. The sample was then annealed twice in ambient air at 900 °C for 5 h and once for 45 h with intermediate hand-grinding and pelletizing, using the same sacrificial powder. The PXRD pattern of the resulting powder shows a mixture of the perovskite phase subsequently identified as $La_3Li_3W_2O_{12}$ and $Li_4WO_5$ impurity (PDF no. 00-021-0530). This impurity can be removed by sonicating the powder in dilute nitric acid (roughly 1 g of powder per 60 mL of a 25 mmol/L solution of $HNO_3$ in water) for 5 min. The powder is then filtered, washed several times with distilled water and left to dry at 100 °C.

*Isotopically Enriched Samples for Neutron Diffraction and NMR.* As $^6$Li has a very large absorption cross section, neutron diffraction experiments were performed on a $^7$Li enriched $La_3Li_3W_2O_{12}$ prepared using the same synthesis pathway and using $^7$Li enriched $Li_2CO_3$ (99% $^7$Li, Sigma-Aldrich, predried at 200 °C) as the lithium precursor. Because of the low NMR receptivity of $^6$Li,[30] $^6$Li enriched $La_3Li_3W_2O_{12}$ ($La_3{}^6Li_3W_2O_{12}$) was also synthesized by using $^6Li_2CO_3$ (99.9% $^6$Li, Sigma-Aldrich, predried at 200 °C). $^{17}$O enriched $La_3Li_3W_2O_{12}$ ($La_3Li_3W_2{}^{17}O_{12}$) was prepared by a gas−solid exchange reaction with $^{17}$O enriched $O_2$ gas (60% $^{17}$O, Sigma-Aldrich, used as received).[31] A sealed quartz tube containing $La_3Li_3W_2O_{12}$ in a $^{17}$O enriched $O_2$ gas atmosphere was heated at 5 °C/min to 600 °C and held for 12 h. The sample was then cooled to room temperature at a rate of 5 °C/min.

*Transmission Electron Microscopy Energy Dispersive X-ray Spectroscopy.* TEM-EDX was performed in a JEOL 2000FX equipped with an EDAX spectrometer. A small amount of powder from each sample was dispersed in a small quantity of ethanol and deposited on a copper TEM grid. Ten particles were chosen at random and analyzed to determine the powder composition, and correction factors obtained from suitable reference compounds were applied to the raw data.



DOI: 10.1021/acs.chemmater.6b03220
Chem. Mater. XXXX, XXX, XXX−XXX

*Compositional Analyses.* Inductively coupled plasma optical emission spectrometry (ICP-OES) was used for compositional analysis. A solution of $La_3Li_3W_2O_{12}$ in $H_2O$ was prepared by dissolving the solid (approximately 60 mg) in 1.1 M of $HNO_3$ (7 mL) and 0.9 M of $H_2O_2$ (3 mL) making up to 100 mL with deionized $H_2O$. Metal contents were corrected for interference by comparing separate and combined metal solutions of known concentrations (25 mg/L). Experiments were performed on a Ciros (Spectro) radial view instrument.

*Dilatometry Measurements.* The measurements for a 6 mm diameter pellet of $La_3Li_3W_2O_{12}$ were performed on a DIL 402C (Netzsch) push-rod dilatometer under ambient air. The pellet was covered in platinum foil to avoid contamination of the alumina spacers. The sample was heated to 700 °C at a rate of 5 °C/min followed by a slower heating rate of 2 °C/min up to 860 °C, followed by a holding time of 24 h at 860 °C before a cooling step at a rate of 5 °C/min down to 50 °C.

**2.2. Diffraction Experiments.** Powder X-ray diffraction (PXRD) data for initial phase identification and indexing were collected in Bragg–Brentano mode on a Panalytical X'Pert Pro diffractometer using monochromated Co $K_{\alpha 1}$ radiation ($\lambda$ = 1.7890 Å). High resolution synchrotron PXRD data (SXRD) were collected at room temperature at beamline I11 (Diamond, UK) with an incident wavelength of 0.826 185(5) Å, using 5 multianalyzer crystal detectors with the sample contained in a spinning borosilicate capillary. Rietveld refinements against SXRD data were carried out using Topas Academic version 5,[32] against data in the $5 \leq 2\theta \leq 90°$ range and using Chebyschev background (18 terms) and Pearson-VII peak profile functions.

High resolution time-of-flight powder neutron diffraction data (PND) were collected at HRPD (ISIS, UK) at room temperature and 5 K from a sample enriched with $^7Li$ to minimize absorption by $^6Li$. Room temperature data were collected from the high resolution back scattering detector bank ($2\theta$ = 168°) using a pulse window of 30–130 ms, corresponding to a *d*-spacing range of $0.6 < d < 2.6$ Å. For the data collection at 5 K, the pulse window was adjusted to 10–110 ms to allow a *d*-spacing range $0.2 < d < 2.2$ Å. In both cases, long data acquisition times were used to ensure adequate counting statistics at the smallest *d*-spacings. All data were corrected for absorption prior to Rietveld analysis. Rietveld refinements against PND data were carried out using GSAS.[33,34]

**2.3. Computational Details.** All calculations were performed using plane-wave based periodic density functional theory (DFT) with the PBE functional.[35] VASP[36] was used for the bulk of calculations, with the projector augmented wave method[37] used to treat core electrons. An energy cutoff of 600 eV was imposed, with *k*-point grids corresponding to a 4 × 4 × 3 grid in the 20 atom experimental cell. Unit cell parameters and atomic positions were optimized until forces on atoms reached 0.01 eV/Å. The relative energies of structures calculated using a larger *k*-point grid (7 × 7 × 5) and tighter force threshold (0.001 eV/Å) differed by less than 0.01 eV/formula unit (FU). Normal mode calculations were carried out at the Γ point using finite differences and the harmonic approximation. Partial occupancies of the electronic states were set using a Gaussian of width 0.01 eV.

Ab initio molecular dynamics (AIMD) calculations were performed using the NVT ensemble, with the cell fixed to the DFT optimized cell parameters of the starting structure. A 1 ps equilibration run was performed with the temperature rescaled at each step to the target temperature. For subsequent production runs, a Nosé thermostat was used, and the charge density recalculated every 1 ps. At high temperatures, a broader 0.1 eV wide Gaussian was used to aid convergence of the electronic states.

Nudged Elastic Band (NEB) calculations were performed with initially six, and then 12 images along each path. The position of one W atom was fixed across the trajectory to prevent translational drift occurring during structural optimization. Cell parameters and atomic positions were optimized until forces on atoms reached 0.01 eV/Å.

NMR parameters were calculated using GIPAW[38,39] as implemented in CASTEP[40] on the three most stable calculated configurations: **C1**, **C2** and **C3** (see below). Before NMR parameters were calculated, structures were reoptimized starting from those obtained using VASP, with a higher cutoff energy of 700 eV, and a force threshold of 0.001 eV/Å. The calculated isotropic magnetic shieldings ($\sigma_{iso}$) were converted to the isotropic chemical shifts ($\delta_{iso}$) to allow comparison with the experimental values using the following expression $\delta_{iso} = 223.7 - 0.888\sigma_{iso}$ for $^{17}O$ shifts[41] and $\delta_{iso} = 86.9 - 0.961\sigma_{iso}$ for $^{6,7}Li$ shifts (see SI). The quadrupole coupling constants are obtained as $C_Q = eQV_{zz}/h$ and the asymmetry parameter as $\eta_Q = (V_{xx} - V_{yy})/V_{zz}$, where an ordering $|V_{zz}| \geq |V_{yy}| \geq |V_{xx}|$ of the principal components of the traceless electric field gradient tensor is assumed.

**2.4. Nuclear Magnetic Resonance Experimental Details.** $^6Li$ magic angle spinning (MAS) solid-state NMR experiments were carried out on a 9.4 T Bruker Avance III HD spectrometer equipped with a Bruker 4 mm HXY MAS probe (in double resonance mode) tuned to X = $^6Li$ at a Larmor frequency $\nu_0(^6Li)$ = 58.88 MHz and on a 20 T Bruker Avance II spectrometer with a Bruker 4 mm HX MAS probe tuned to $^6Li$ at $\nu_0(^6Li)$ = 125.11 MHz. $^6Li$ spectra were obtained with a $\pi/2$ pulse length of 3 $\mu$s at a radio frequency (rf) amplitude of $\nu_1(^6Li)$ = 83 kHz at a MAS rate of 10 kHz. Additional $^6Li$ MAS NMR spectra were recorded on the same 9.4 T NMR spectrometer with a Bruker 1.3 mm HXY MAS probe at with a $\pi/2$ pulse length of 3 $\mu$s at a rf amplitude of $\nu_1(^6Li)$ = 83 kHz at a MAS rate of 60 kHz.

$^{17}O$ rotor synchronized Hahn echo and two-dimensional (2D) z-filtered multiple-quantum MAS (MQMAS)[42−44] experiments were carried out on a 9.4 T Bruker Avance III HD spectrometer with a Bruker 4 mm HXY MAS probe (in double resonance mode) tuned to $^{17}O$ at $\nu_0(^{17}O)$ = 54.2 MHz and at a MAS rate of 13 kHz, and on a 20 T Bruker Avance II spectrometer with a Bruker 3.2 mm HXY MAS probe (in double resonance mode) tuned to $^{17}O$ at $\nu_0(^{17}O)$ = 115.3 MHz and at a MAS rate of 20 kHz. $^{17}O$ spectra were obtained with $\pi/2$ pulse lengths of 1 and 1.2 $\mu$s at a rf amplitude of $\nu_1(^{17}O)$ = 83 and 70 kHz at 20 and 9.4 T, respectively. Excitation and reconversion pulses in the 2D $^{17}O$ 3QMAS NMR experiments were performed at rf amplitude of $\nu_1(^{17}O) \approx 83$ kHz, whereas the selective $\pi/2$ was obtained at 13 kHz.

All variable temperature $^6Li$ and $^7Li$ solid-state NMR experiments were obtained under static conditions at 9.4 T and with $\nu_0(^6Li)$ = 58.88 MHz and $\nu_0(^7Li)$ = 155.51 MHz, respectively. Below 650 K, experiments were conducted on a 9.4 T Bruker Avance III HD spectrometer with a Bruker 4 mm HX high temperature MAS probe (between 294 and 650 K) and with a Bruker 4 mm HXY MAS probe (in double resonance mode) below 294 K using standard 4 mm $ZrO_2$ rotors and caps. Above 650 K, experiments were carried out on a 9.4 T Bruker Avance spectrometer using a single channel high temperature static NMR probe with a homemade $CO_2$ laser ($\lambda$ = 10.6 $\mu$m, 250 W) heating system developed in Orléans (CNRS–CEMHTI, France).[45,46] The sample was placed in a BN crucible and inserted into the rf coil of the high temperature NMR probe. The sample is heated up by two lasers, passing axially through the NMR probe, with the sample temperature controlled by the laser power output. A flow of $N_2$ is used to cool the rf coil and a flow of Ar gas to prevent oxidation of the BN crucible at high temperature. $^6Li$ spectra were obtained with a $\pi/2$ pulse of 3 $\mu$s at an rf amplitude of $\nu_1(^6Li)$ = 83 kHz below 650 K and with a $\pi/2$ pulse of 52.5 $\mu$s at an rf amplitude of $\nu_1(^6Li)$ = 4.7 kHz above 650 K. $^7Li$ spectra were obtained with a $\pi/2$ pulse of 2 $\mu$s at an rf amplitude of $\nu_1(^7Li)$ = 62.5 kHz below 650 K and with a $\pi/2$ pulse of 8 $\mu$s at an rf amplitude of $\nu_1(^7Li)$ = 15 kHz above 650 K. Spin–lattice relaxation times in the laboratory frame ($T_1$) were obtained using a saturation recovery pulse sequence and the data were fitted to a stretched exponential of the form $1 - \exp[-(\tau/T_1)^\alpha]$, where $\tau$ are variable delays and $\alpha$ is the stretch exponential coefficient (between 0.85 and 1). $^7Li$ spin–lattice relaxation times in the rotating frame ($T_{1\rho}$) were obtained with a spin-lock pulse sequence at frequencies of $\nu_1(^7Li)$ = 8 and 14 kHz. $T_{1\rho}$ data were fitted to a stretch exponential of the form $\exp[-(\tau/T_{1\rho})^\alpha]$. Temperature calibrations of the MAS probes (below 650 K) were performed with the $^{207}Pb$ chemical shift thermometer of $Pb(NO_3)_2$,[47,48] and by following the $^{63}Cu$ resonances of $Cu^I$I and $Cu^I$Br across the $\gamma$-to-$\beta$ phase transition at 642 and 658 K, respectively.[49,50] Temperature calibration of the laser heated NMR probe was carried out by direct measurements of the melting points of


DOI: 10.1021/acs.chemmater.6b03220
Chem. Mater. XXXX, XXX, XXX−XXX

reference samples.[45,46] All temperatures reported are actual sample temperatures and have an estimated accuracy of ±5 K (below 294 K), ±10 K (between 294 and 420 K, ±20 K (between 420 and 600 K) and ±30 K (above 600 K on the static laser probe).

Spectra were referenced to 10 M LiCl in $D_2O$ (for $^{6,7}Li$ shifts) and $H_2O$ (for $^{17}O$ shifts) at 0 ppm.

**2.5. Processing and AC Impedance Spectroscopy.** The synthesized powder samples were ball-milled overnight in ethanol (350 rpm, Fritsch Pulverisette 7 Planetary Mill) and dried at 350 °C under flowing dry $O_2$ for 24 h. The powders were then pressed uniaxially in to pellets of 10 mm diameter and subjected to isostatic pressing at 200 MPa using an Autoclave Engineers Cold Isostatic Press. The resulting pellets were sintered at 900 °C under $O_2$ for 36 h, and a density of ≈67% was obtained. X-ray diffraction showed no impurity phases were present in the pellet. The samples were coated with Ag paste, followed by heating to 100 °C for 1 h to ensure bonding to the sample surface. Conductivity measurements were then performed in dry, ambient and wet air (the inlet gas being bubbled through water at room temperature resulting in water partial pressure of $P_{H2O} \approx 0.03$ atm) by AC impedance spectroscopy (Solartron 1260A impedance analyzer) in the frequency range from 0.01 to $3 \times 10^7$ Hz with a perturbation of 20 mV. The impedance data were analyzed using ZView software.

## 3. RESULTS

**3.1. Synthesis and Chemical Analysis.** Initial synthetic effort concentrated on the introduction of A-site vacancies into $SrLi_{0.4}W_{0.6}O_3$[24] with the aim of subsequently filling them partially with Li. This was addressed by replacing $Sr^{2+}$ with 2/3 $La^{3+}$ to form the series $Sr_{1-3x/2}La_xLi_{0.4}W_{0.6}O_3$. These reactions led to multiphase products, but it was noted that solid state reactions at the target composition $La_{2/3}Li_{0.4}W_{0.6}O_3$ with a large amount of excess Li to avoid Li loss during synthesis resulted in the formation of $Li_4WO_5$ and a new phase matching a monoclinic distorted perovskite by indexing the PXRD pattern. Sonication in nitric acid converted the $Li_4WO_5$ to the water-soluble $Li_2WO_4$, allowing purification of the perovskite phase by washing in water. Initial ICP-OES and TEM-EDX analysis suggested that this phase had a composition close to $La_3Li_3W_2O_{12}$, and subsequent synthesis at 900 °C for 65 h from oxide starting materials at this nominal composition resulted in phase pure samples without the need for the removal of impurities by washing. This synthetic route was used for all materials measured in the paper.

The metal content of $La_3Li_3W_2O_{12}$ was measured by ICP-OES, and after normalizing the metal concentrations to a total of eight cations, the determined composition is $La_{3.020(81)}Li_{2.975(61)}W_{2.004(9)}$ (Table S1 in the Supporting Information). In addition, TEM-EDX analysis was used to measure the La/W ratio of ten individual grains of the same sample, and shows a distribution of La/W ratios with a mean of 1.52(8) (Figure S1). The nominal stoichiometric composition of $La_3Li_3W_2O_{12}$ lies within the standard deviation of the composition measured by both ICP-OES and TEM-EDX, and will be used throughout the rest of the paper.

**3.2. Diffraction Experiments.** *3.2.1. Cell Indexing and B-Site Cation Ordering by Powder X-ray Diffraction.* The reflections from the room temperature SXRD pattern of $La_3Li_3W_2O_{12}$ were indexed to a monoclinic cell represented by a $\sqrt{2}a_p \times \sqrt{2}a_p \times 2a_p$ expansion of the cubic perovskite subcell (of lattice parameter $a_p$), and its systematic absences were found to be consistent with space group $P2_1/n$. A corresponding Pawley refinement fitted all of the observed peaks with refined unit cell dimensions $a$ = 5.544 35(3) Å, $b$ = 5.611 14(3) Å, $c$ = 7.888 43(4) Å and $\beta$ = 90.0982(2)° (Figure S2). The small monoclinic distortion is difficult to resolve by laboratory PXRD but is clearly resolved by SXRD (e.g., the splitting of the 101 and $10\bar{1}$ peaks, see inset in Figure S2). The combination of a monoclinic $\sqrt{2}a_p \times \sqrt{2}a_p \times 2a_p$ unit cell with $P2_1/n$ symmetry is characteristic of cryolite-type double perovskites, where 1:1 (rock-salt type) B cation ordering (further confirmed by the presence of $(0kl)$: $k = 2n+1$ reflections) is combined with a small tolerance factor that induces a $b^-b^-c^+$ type octahedral tilt distortion.[51] The Li containing double perovskite $La_2LiSbO_6$[27] is an example of this class of double perovskites: it contains $Li^+$ and a high valency cation ($Sb^{5+}$) in a 1:1 ratio on the B sublattice, whereas the A-site is rich in $La^{3+}$. Consequently the structure of $La_2LiSbO_6$[27] was used to derive a preliminary Rietveld model of $La_3Li_3W_2O_{12}$, with $Sb^{5+}$ replaced by $W^{6+}$ and the single crystallographically independent A-site populated by La only (in this refinement the occupancy of Li was ignored due to the insensitivity of X-rays to scattering by Li in the presence of W and La). In order to minimize correlation with refined occupancy parameters, constraints were then applied to the thermal parameters such that the three oxide sites were described by a single parameter, and the B-site cations were also described by a single parameter (due to the weak scattering power of Li). Initially, the atomic coordinates and isotropic thermal parameters were refined, with site occupancies fixed to nominal values. The Li/W occupancies of the B-sites were then allowed to refine independently, with the total occupancy at each site constrained to 1, with no constraint on the global composition. The resulting Rietveld fit is shown in Figure 1a, and the final refined parameters are shown in Table S2. These indicate that the B-site Li/W cations are fully ordered, with refined compositions of $Li_{1.000(1)}W_{0.000(1)}$ (2c site) and $Li_{0.015(3)}W_{0.985(3)}$ (2d site) respectively. The refined La/W ratio of 1.522(4) is consistent with the nominal composition and that determined by TEM-EDX and ICP-OES experiments.

*3.2.2. Location of A-Site $Li^+$ Ions by Powder Neutron Diffraction.* The low concentration of $Li^+$ ions on the A-site, coupled to their weak X-ray scattering power, precludes their location by PXRD. However, it has proven to be possible to locate partially occupied Li sites in similar systems, such as $La_{0.567}Li_{0.3}TiO_3$, by using high resolution neutron diffraction (and hence a stronger negative scattering factor for Li) to generate Fourier difference maps.[52] The provisional structural model obtained by Rietveld refinement against SXRD data (see section 3.2.1), with no Li on the A-site, was used as a starting model in a Rietveld refinement against HRPD neutron diffraction data collected at 5 K in the $d$-spacing range 0.5−2.1 Å, and also the room temperature data set in the $d$-spacing range 0.6−2.6 Å, using only the high resolution detector bank (similar to the strategy employed for $Li_{0.30}La_{0.567}TiO_3$[52]). The atomic coordinates were refined independently for La and the three oxide sites and isotropic displacement parameters were refined independently for all atoms. This provided a reasonable fit to both data sets ($R_{wp}$ = 2.21%, $\chi^2$ = 3.15 at 5 K and $R_{wp}$ = 4.67%, $\chi^2$ = 8.29 at room temperature, see Figure S3). Inspection of the corresponding Fourier difference maps (Figure 2) revealed a single intense negative peak at 5 K, indicative of unmodelled scattering from Li, which is displaced from the La site by 1.03(2) Å approximately parallel to the $[010]_p$ direction. The large displacement of this peak from the La position, and its negative intensity, means that it cannot be accounted for by disorder (either static or dynamic) of the La position. A negative peak was also found at this position in the


DOI: 10.1021/acs.chemmater.6b03220
Chem. Mater. XXXX, XXX, XXX−XXX

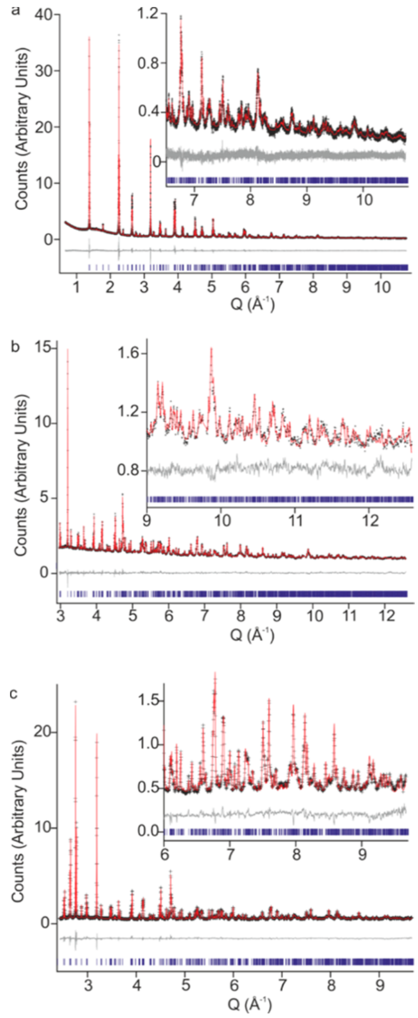


**Figure 1.** Rietveld refinements of $La_3Li_3W_2O_{12}$. (a) Simplified structural model (i.e., no A-site Li) refined against high resolution synchrotron X-ray diffraction at ambient temperature. (b) Refinement of the full structural model against PND data from the backscattering bank of HRPD, using a time-of-flight window of 10−110 ms at 5 K. (c) Refinement of the same structural model against PND data from the same detector bank, using a time-of-flight window of 30−130 ms at ambient temperature.

Fourier difference map generated at room temperature, but at this temperature it is difficult to distinguish it from the background features (see Figure 2c): consequently, the 5 K data were used to locate the Li coordinates with greater precision. The model was modified to include Li on this position with an occupancy of 0.25, corresponding to the nominal composition. Isotropic displacement parameters ($U_{iso}$) were refined independently for each atom, and atomic coordinates for La, Li1 (A-site) and the three oxide sites were also refined independently. The site occupancies were fixed to nominal values for all atoms, as the simultaneous refinement of the occupancy and $U_{iso}$ for Li1 was precluded by a strong correlation between these parameters. This produced a stable refinement (Figure 1b) with an improvement of fit ($R_{wp}$ = 2.15%, $\chi^2$ = 2.969) for which the refined structural parameters are given in Table S3. Attempts to include Li on other, weaker, negative peaks in the Fourier difference map did not produce stable refinements. The resulting model has A-site Li displaced from the centroid of the $O_{12}$ cage by 0.79(2) Å along the $(110)_p$ direction, where it is coordinated to 4 nearest-neighbor oxygens in a distorted tetrahedron, with Li−O distances in the range 2.11(2)−2.20(2) Å (Figure 3). Calculation of the bond valence sums (BVS)[53] at the Li sites gives values of 1.00 at the $LiO_6$ B-site, and 0.62 at the $LiO_4$ A-site, indicating that Li is under-bonded in this position. However, this agrees closely with the structure predicted by DFT calculations (Figure 4, see below), implying that this is the most stable position available for A-site Li.

After the $Li^+$ ions were located at 5 K, the model was tested against room temperature data (Figure 1c). The atomic coordinates and isotropic displacement parameters of the Li1, La and the oxide ions were refined independently, with site occupancies fixed to nominal values, and this was found to produce a stable refinement and an improved fit ($R_{wp}$ = 4.54%, $\chi^2$ = 7.842). Attempts to include Li atoms on the sites of other negative peaks resulted in unstable refinements with the A-site Li showing a strong tendency to move far from its initial position, and these models were therefore discarded. The refined room temperature structural parameters are shown in Table S4, and the structure (which is isostructural with the 5 K model) is illustrated with the local coordination of A-site Li in Figure S4. Note that, for clarity, the detailed discussion of the $La_3Li_3W_2O_{12}$ structure (section 4) refers only to the 5 K model.

**3.3. Computation.** *3.3.1. Location of A-Site Li.* The experimentally determined unit cell of $La_3Li_3W_2O_{12}$ contains four A-sites, three occupied by La on average, and one by Li. To aid in the determination of the likely location of A-site Li in $La_3Li_3W_2O_{12}$, DFT calculations in the crystallographic unit cell were performed starting from the refined structure of $La_3Li_3W_2O_{12}$, with a single A-site Li initially placed on the same site as determined for La. Upon structural relaxation, the A-site Li was displaced away from the La site by 0.4 Å along the *b* axis to a new site, **A1** (Figure 4a,b), close to that determined by low temperature PND. In this site, which is 4-fold coordinated to O atoms, Li sits in the base of a distorted tetrahedron, with three short bonds (2.00, 2.04 and 2.08 Å), and one long bond to the apex of the tetrahedron (2.39 Å). The calculated BVS for Li at **A1** is 0.77, slightly lower than that of the two B-site Li atoms (0.81 and 0.90). As DFT calculations using the generalized gradient approximation are known to overestimate bond lengths, and consequently underestimate BVS, site **A1** appears to be a reasonable coordination environment for the A-site Li. No normal modes with imaginary frequencies are calculated for this structure, showing that it is a true minimum on the potential energy surface at 0 K.

AIMD calculations were performed to investigate the possibility that Li may reside in different coordination environments within a single $O_{12}$ cage around the A-site. Taking the previously calculated cell with Li on site **A1**, a 23 ps AIMD run was performed at room temperature (298 K) using a 1 fs time-step. The trajectory of the A-site Li atom clearly shows that the atom does not simply oscillate around site **A1**, rather it is able to access a large region of space around the center of the $O_{12}$ cage (Figure 4c). A Li density map was constructed, by placing a Gaussian function at each point in space visited by Li during the 23 ps trajectory (Figure 4d). This map, which reflects the amount of time spent by Li in any location, shows that there are other sites in which the A-site Li spends an appreciable amount of time.

Performing standard structural optimization calculations with the A-site Li on these sites within the $O_{12}$ anion cage, followed by normal mode calculations, results in the determination of


DOI: 10.1021/acs.chemmater.6b03220
Chem. Mater. XXXX, XXX, XXX−XXX

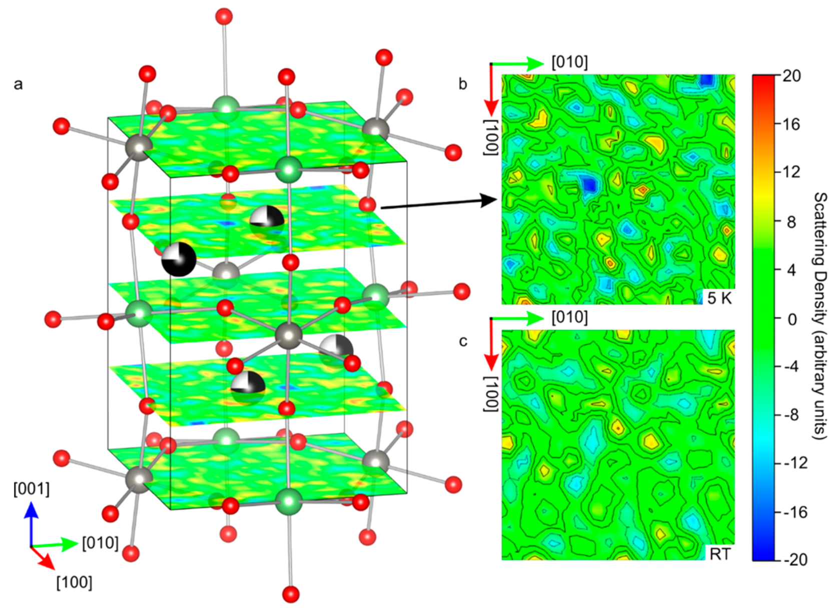


**Figure 2.** (a) Neutron diffraction Fourier difference map of $La_3Li_3W_2O_{12}$ sliced in the (001) plane, resulting from a Rietveld model with no A-site Li atoms (superimposed on the map), refined against PND data at 5 K. Atom colors: La in black, Li in green, W in gray, O in red. (b) Individual slice through $z$ = 0.75 at 5 K, showing an intense negative peak (blue) which corresponds to unmodelled Li scattering intensity on the A-site. (c) Individual slice through $z$ = 0.75 at ambient temperature, resulting from a Rietveld model with no A-site Li atoms, showing only weak negative peaks that are difficult to distinguish from the background.

two more A-site positions which are minima on the 0 K potential energy surface, **A2** and **A3** (Figure S5). The $La_3Li_3W_2O_{12}$ structure with A-site Li on either of these two sites is 0.04 eV/FU higher in energy than with Li in **A1**, but at room temperature AIMD shows that all three sites are occupied for some time. The A-site Li is coordinated to four O atoms on site **A2** as on site **A1**, but Li on site **A3** has three short Li−O bonds forming a roughly trigonal planar geometry (Figure S5), though three longer Li−O distances between 2.6 and 3.0 Å may also contribute to stabilizing Li on this site. Nudged elastic band (NEB) calculations were performed to determine the barriers to Li atom hopping between sites **A1**, **A2** and **A3**. The calculated barriers between **A1** and **A2**, and **A1** and **A3** are 0.08 and 0.07 eV/FU, respectively (Figure 4e). These barriers are around $3k_BT$ at room temperature, and small enough to allow appreciable hopping between sites even on the picosecond time scale.

*3.3.2. Local A-Site Ordering.* Refinement of SXRD data shows that the La atoms are randomly distributed over all A-sites, with a partial occupancy of 0.75. There is often a trend toward La ordering in related systems,[9,53−58] though this sometimes only seen at the local scale.[59] To assess the likelihood of local A-site ordering between La and Li in $La_3Li_3W_2O_{12}$, 128 unique La/Li distributions were generated in a 2 × 2 × 1 supercell using the site occupancy disorder program,[60] and the resulting supercells structurally optimized using DFT.

Configurations **C1** and **C2**, along with the next most stable configuration, **C3** (Figure S6), were used to calculate $^6$Li and $^{17}$O NMR parameters for comparison with the experimental results in section 3.4.

The energies of the configurations are distributed over a relatively small energy range of 0.43 eV/FU. Two energetically degenerate configurations are found to be the most stable, **C1** and **C2** (Figure 5). Both configurations show ordering of A-site Li into distinct columns through the structure, running along the $b$ axis in **C1** and the $c$ axis in **C2**, resulting in A-site layers which are fully occupied by La. The alternation of fully La occupied A-site layers with mixed La/Li or La/vacancy layers has been observed in related perovskites, with long-range ordering present in $La_{2/3-x}Li_{3x}TiO_3$, $La_{1/3}NbO_3$,[55] $La_4Mg_3W_3O_{18}$[56] and $La_6Mg_4Ta_2W_2O_{24}$,[61] and short-range ordering present in $La_{5/3}MgTaO_6$.[59] A comparison of other computed configurations of $La_3Li_3W_2O_{12}$ shows that arrangements in which A-site Li are well separated are generally higher in energy. Assuming a completely random distribution of La and Li on the A-site, each A-site Li would be expected to have an average of 0.75 out of six nearest-neighbor A-sites occupied by Li. A plot of configuration energy versus the average number of Li A-site nearest-neighbors for each Li within a configuration, shows a clear trend, with a low $p$-value (probability of no correlation) of 2 × $10^{-9}$, toward higher numbers of Li−Li nearest neighbors in more stable configurations (Figure 5). This suggests a preference toward local ordering of La and Li. However, the relatively smooth distribution of configuration energies, and the large number of different configurations within $k_BT$ at the synthetic temperature, prevents long-range ordering into any single ordered configuration, and hence the average structure has a three-dimensional Li distribution.

*3.3.3. Generation of A-site Li Vacancy Defects.* Motion of Li through $La_3Li_3W_2O_{12}$ is likely to require the presence of Li vacancy defects within the structure. A-site vacancies in stoichiometric $La_3Li_3W_2O_{12}$ can be created by hosting two Li atoms on the same A-site. The energy cost of creating such Frenkel defects was calculated by taking configurations **C1** and **C2** in the 2 × 2 × 1 supercell, and moving one A-site Li atom away from its original site into a site close to another A-site Li atom. After relaxing seven such structures using DFT, the lowest energy structure, a defective **C2** configuration (Figure 5e), was 0.39 eV per defect higher in energy than the perfect **C2** configuration. The two A-site Li atoms within the same A-site $O_{12}$ cage are located close to the **A1** and **A2** positions


DOI: 10.1021/acs.chemmater.6b03220
Chem. Mater. XXXX, XXX, XXX−XXX

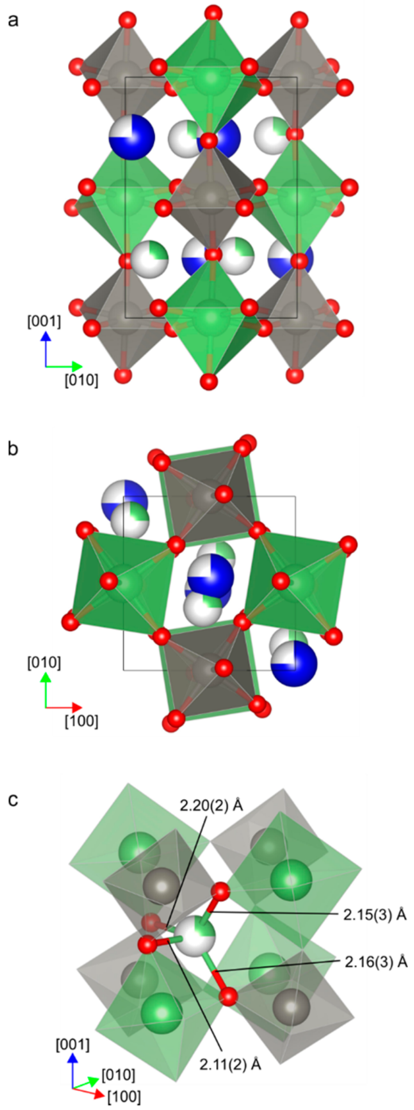


**Figure 3.** Crystal structure of $La_3Li_3W_2O_{12}$ from NPD at 5 K. (a) Monoclinic $\sqrt{2}a_p \times \sqrt{2}a_p \times 2a_p$ unit cell viewed along the (100) axis. (b) Unit cell viewed along the (001) axis. (c) A fragment of the unit cell showing the distorted tetrahedral coordination of Li at the A-site. Atom colors: La in blue, Li in green, W in gray, O in red; pie charts signify the occupancies of the sites.

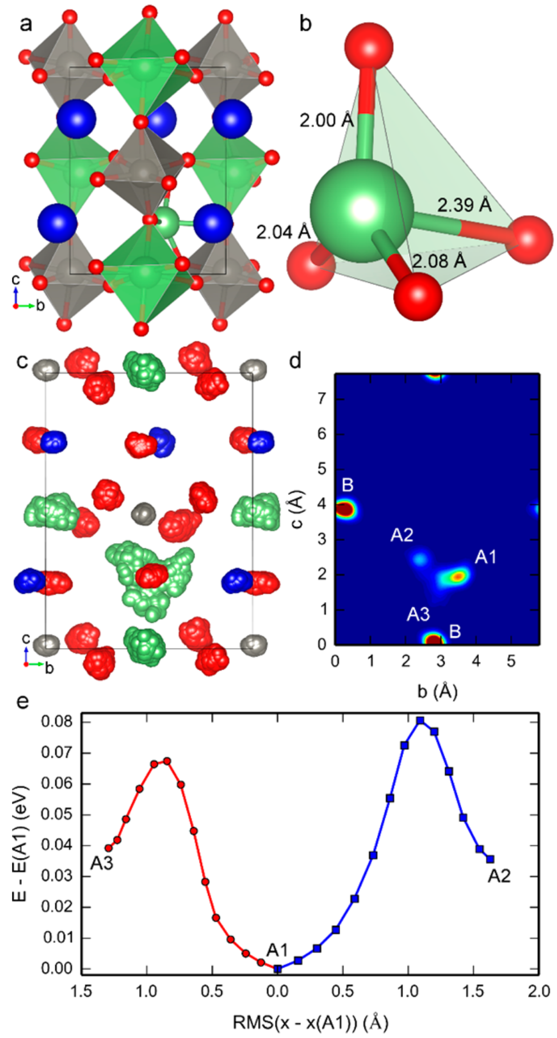


**Figure 4.** A-site Li positions in $La_3Li_3W_2O_{12}$ calculated by DFT. Position **A1** is shown in panel a, and the coordination spheres of the A-site Li atom are labeled with Li−O distances below 2.5 Å in panel b. The atomic positions during a 23 ps trajectory of a room temperature AIMD run are plotted every 10 fs in panel c. A Li density map of this trajectory in panel d shows that the A-site Li resides in different positions within the cell. These are labeled according to the corresponding stable A-site positions determined by DFT: **A1**, **A2** and **A3**. Atom colors: La in blue, Li in green, W in gray, O in red. The energies of the lowest energy pathways between site **A1** and sites **A2** and **A3** were calculated using the NEB method, and are plotted in panel e as a function of the root-mean-square difference in positions between each image structure and the lowest energy structure, **A1**.

(section 3.3.1), though displaced away from each other increasing the Li−Li separation to 2.6 Å (Figure 5e).

A-site vacancies could also be generated by a slight excess of La (within the experimental uncertainty), forming $La_{3+x}Li_{3-3x}W_2O_{12}$. Starting from configuration **C1** (section 3.3.2), 55 symmetrically unique configurations were generated in the 2 × 2 × 1 supercell, in which one A-site Li atom was replaced with a La atom, and two A-site Li atoms removed. These configurations were relaxed using DFT, and energetically compared to a combination of $La_3Li_3W_2O_{12}$ and $La_2WO_6$. The lowest energy configuration (Figure 5f) gives a defect energy of 0.77 eV per additional La atom, or equivalently 0.39 eV per Li vacancy.

Charge compensation of two Li vacancies by removal of a single oxide ion was investigated by calculating the energy of 40 unique arrangements of Li and O vacancies starting from configuration **C1**. The lowest energy arrangement (Figure 5g) contains a 5-fold coordinated W atom, in a trigonal bipyramidal coordination geometry. It is 1.11 eV less stable than the defect free structure, a defect energy of 0.55 eV per Li vacancy.

Another potential compensation mechanism is the replacement of a B-site Li with a B-site W, and five A-site Li vacancies, but it is not feasible to model this using the present supercell methodology. By necessity, the calculations presented here are performed in relatively small supercells, and therefore represent an unrealistically high defect concentration, nevertheless they reveal that Li vacancies can be formed with an energy penalty below $5k_BT$ at the synthesis temperature of $La_3Li_3W_2O_{12}$, and are therefore likely to exist at low concentrations.

*3.3.4. Li Motion between $O_{12}$ Cages.* The motion of A-site Li atoms between neighboring $O_{12}$ cages was investigated by performing a 20 ps AIMD run at 673 K within a supercell


DOI: 10.1021/acs.chemmater.6b03220
Chem. Mater. XXXX, XXX, XXX−XXX

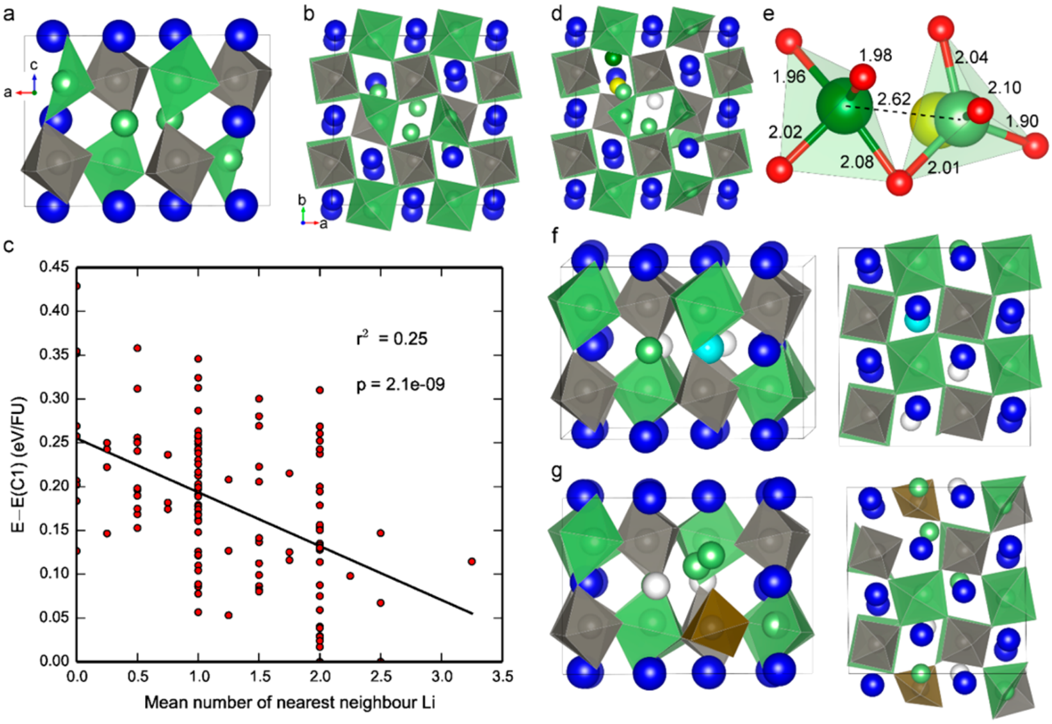


**Figure 5.** Two most stable arrangements of A-site La and Li in a 2 × 2 × 1 supercell and the computed structure of Li vacancy defects: (a) configuration **C1** and (b) configuration **C2**. Structures are viewed down the axis along which A-site Li forms columns, with the A-site Li in the center of the cell. A-site layers fully occupied by La can be seen at the edges of the cells. B-site atoms and their coordinating O atoms are shown as polyhedra. (c) The energy of 128 configurations relative to configuration **C1** is plotted against the mean number of Li A-site nearest neighbors for each A-site Li within the structure. The black line is a fit by linear regression to the data, showing correlation between the stability of configuration and short-range ordering of the A-site Li atoms. A random distribution of La and Li on the A-site gives a value of 0.75 for the number of nearest neighbors, and Li in 1D columns have two Li A-site nearest neighbors. (d) Frenkel defect in configuration **C2**. The Li vacancy site is shown in white, the new interstitial Li A-site in dark green, and the original A-site Li position in yellow. The coordination environments of the two Li sharing the same A-site are shown in panel e, with bond distances and the Li−Li separation shown in Angstroms. (f) Three A-site Li atoms in configuration **C1** are replaced with one La (cyan) and two vacancies (white). (g) Two A-site Li vacancies (white) in configuration **C1** are compensated by the removal of one oxygen atom, forming a 5-fold trigonal bipyramid coordinated W atom (brown). B-site atoms and their coordinating O atoms are shown as polyhedra. Atom colors: La in blue, Li in green, W in gray. Oxygen atoms have been omitted for clarity, except in panel e where they are shown in red.

containing a Frenkel defect. The vacancy and interstitial Li atoms were separated sufficiently to prevent recombination and removal of the defect. Figure 6 shows that even on the relatively small time scale of 20 ps, hopping between occupied and vacant A-sites in neighboring $O_{12}$ cages is observed, along with considerable motion of the interstitial Li atom within each cage. Cage-to-cage hopping occurs through a window of four O atoms in a roughly rhomboid configuration. Frenkel defects will thus give rise to long-range diffusion at temperatures where finite ionic conductivity is observed in experiment. In addition a single hopping event was observed from an occupied Li B-site to a neighboring vacant A-site and back again (Figure 6c), showing that exchange between the A-site and B-site is possible at this temperature.

To investigate the energetics of $Li^+$ ion hopping in more detail, a series of constrained DFT relaxations were performed. The position of a W atom and the *y*-coordinate of the A-site Li atom in the channel containing the A-site vacancy were fixed in the supercell used in the AIMD run described above. The cell and all other atomic positions were then allowed to relax. This process was repeated for a range of *y*-coordinates through the supercell (Figure 6d), producing an energy landscape for the motion of Li through the two A-sites (Figure 6e). The landscape is more complicated than might be expected, consisting of multiple minima and energy barriers, the configurations of which are shown in Figure S7. The difference in energy between the lowest energy minima and the highest point on the landscape is ∼0.25 eV, with barriers to individual hopping events in the range of 0.1−0.2 eV. Cage-to-cage hopping of Li atoms is therefore likely to occur through a complicated combination of many shorter range hopping processes between local minima on the energy landscape, rather than single hops between one $O_{12}$ cage and the next. This is consistent with the different stable A-site positions within a single cage calculated in section 3.3.1, and the trajectories shown in the AIMD run (Figure 6a).

**3.4. NMR.** Solid state NMR has proven itself to be a valuable technique to investigate and understand Li environments and diffusion in fast $Li^+$ ion conductors, taking advantage of the two stable NMR active isotopes of lithium ($^6Li$ and $^7Li$). $^6Li$ solid-state magic angle spinning (MAS) NMR is widely used for structure investigation because of the high resolution data usually obtained with this isotope. Additionally, it is well-known that there is a correlation between $^6Li$ shift and Li−O coordination[30,62,63] that permits the characterization of the local Li environments. The Li dynamics are studied with a range of $^6Li$ and $^7Li$ variable temperature NMR experiments.[8,64−70] The temperature dependence of NMR line width and spin−lattice relaxation times $T_1$ and $T_{1\rho}$ for both Li nuclei are very sensitive to the mobility of $Li^+$ on the NMR


DOI: 10.1021/acs.chemmater.6b03220
Chem. Mater. XXXX, XXX, XXX−XXX

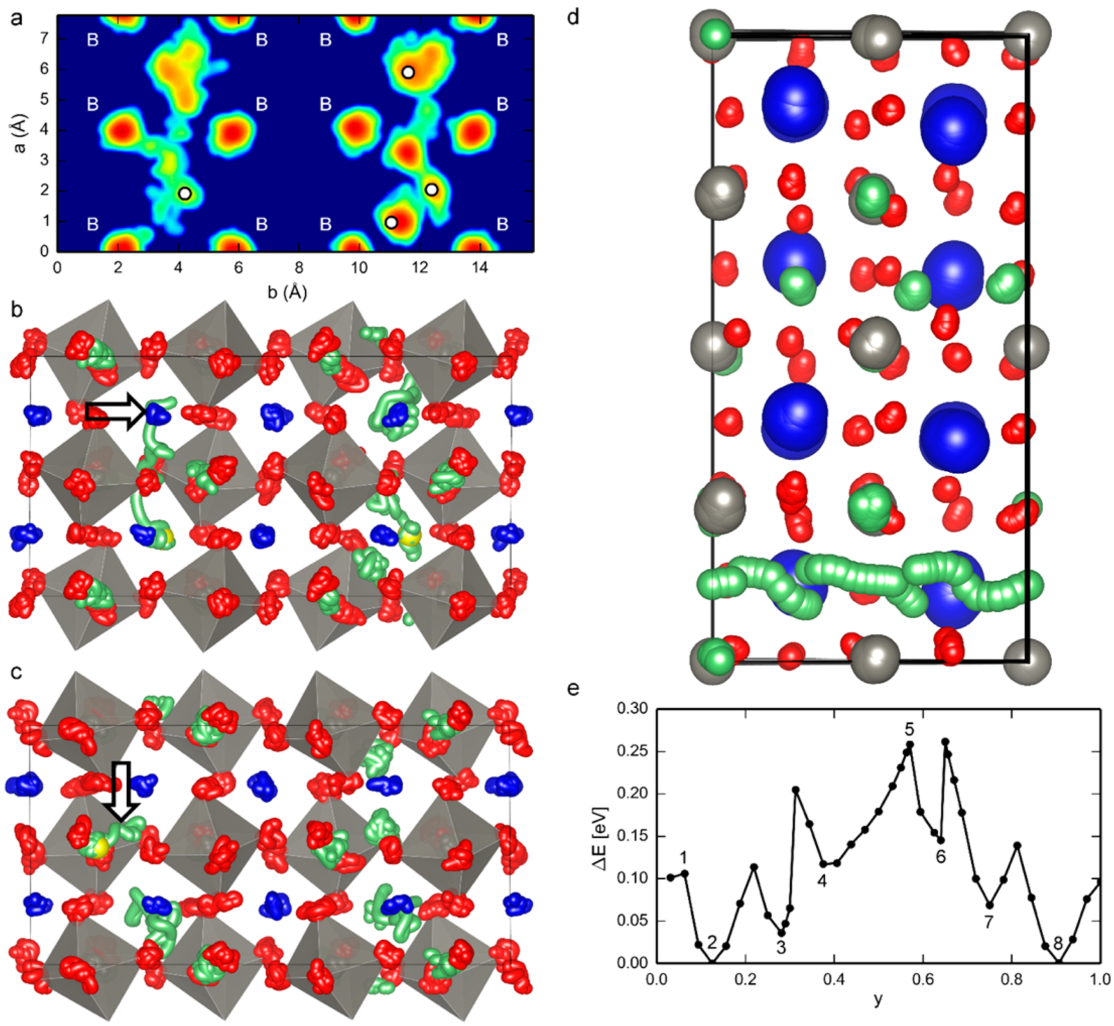


**Figure 6.** Calculated $Li^+$ ion dynamics. (a) A Li density map of the Li positions throughout a 20 ps AIMD run at 673 K. The initial locations of A-site Li atoms are shown as white circles. The left half of the cell contains a vacant A-site, and the right half an interstitial A-site Li. B-site Li atoms are labeled with a B. Contours are plotted on a logarithmic scale. (b) The atomic positions between 3 and 4 ps, showing the migration of A-site Li from an occupied $O_{12}$ cage to a vacant one (left, initially vacant site marked with an arrow) and between two interstitial sites within an $O_{12}$ cage (right). (c) The atomic positions between 15 and 16 ps, showing the migration of a B-site Li (yellow sphere) to the neighboring A-site (Li path marked with an arrow). The energy landscape for the migration of Li through two A-sites is calculated with constrained DFT relaxations. (d) The atomic positions from each constrained DFT relaxation are overlaid as the Li was moved through the A-site channel containing an A-site vacancy, showing the path of Li throughout the cell between two $O_{12}$ cages. (e) The relative energy of each relaxed structure is plotted against the fractional *y*-coordinate of the constrained Li atom. Numbers relate to the atomic configurations shown in Figure S7. Gray polyhedra are the coordination environments of the W atoms, O atoms are shown in red, La in blue and Li in green with yellow spheres marking the positions of the Li atoms at the start of the AIMD run.

time scale (kHz to MHz), allowing determination of Li jump rates $\tau^{-1}$.

*3.4.1. Identification of Two Li Sites with $^6$Li MAS NMR Spectroscopy.* The room temperature $^6$Li MAS NMR spectrum of $La_3{}^6Li_3W_2O_{12}$ recorded at 20 T is presented in Figure 7 (and Figure S8), where two Li environments are clearly observed. The spectrum is fitted with two resonances at 0 and −0.4 ppm in a 1:2 ratio, consistent with the A:B site Li ratio proposed in the structural model. Based on the known relationship between $^6$Li shift and Li coordination numbers,[30,62,63] the latter resonance is assigned to $LiO_6$ whereas the former corresponds to a lower coordinate Li environment. Spectral assignment of this resonance to a specific coordination number is not straightforward given the range of potential shifts for four and five coordinated $Li^+$ ions. For example, $LiO_4$ and $LiO_5$ sites appear at 0.8 and 0.2 ppm in $Li_4SiO_4$ respectively,[62,63] whereas $LiO_4$ appears around 0.1 ppm in other Li containing silicates.[63] These data confirm the presence of both Li atoms in the B-site ($LiO_6$) and the A-site ($LiO_4$ or $LiO_5$) of $La_3Li_3W_2O_{12}$, consistent with both the experimental diffraction and computational DFT determination of the A-site Li coordination environment.

The three most stable configurations of $La_3Li_3W_2O_{12}$ in the 2 × 2 × 1 supercells **C1**, **C2** and **C3** (section 3.3.2) were used to predict the $^6$Li NMR parameters using the GIPAW approach.[38,39] $Li^+$ ions at the A-sites in these optimized structures have calculated isotropic shielding values, $\sigma_{iso}$, of 91.0 ± 0.1 ppm (and calculated isotropic chemical shifts $\delta_{iso,cs}$ = −0.6 ppm) and those at the B-sites of 91.5 ± 0.1 ppm (and $\delta_{iso,cs}$ = −1.0 ppm, Figure S10). Because the experimentally observed shifts are expected to be proportional to $-\sigma_{iso}$,[71] this

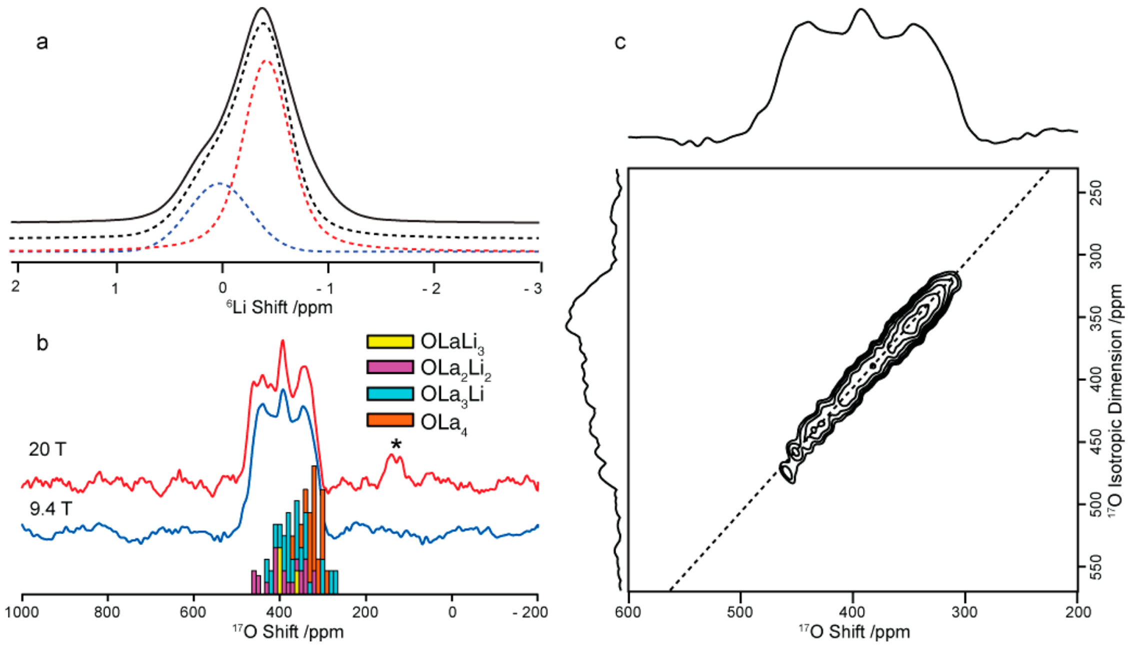


**Figure 7.** NMR structural investigation of $La_3Li_3W_2O_{12}$. (a) $^6$Li magic angle spinning (MAS) NMR spectra of $La_3{}^6Li_3W_2O_{12}$ recorded at 20 T under MAS at 10 kHz. Black dashed lines represent line shape simulation using two different $^6$Li resonances at 0 ppm (blue dashed line) and −0.4 ppm (red dashed line) corresponding to A-site ($LiO_4$ or $LiO_5$) and B-site ($LiO_6$) local environments, respectively. $^6$Li MAS NMR spectra recorded at 9.4 T and faster MAS are given in Figure S8. (b) $^{17}$O Hahn echo NMR spectra of $La_3Li_3W_2{}^{17}O_{12}$ recorded at 9.4 T under MAS at 13 kHz (blue) and at 20 T under MAS at 20 kHz (red). The histogram represents the number of oxygen atoms as a function of the calculated GIPAW[38,39] $^{17}$O shifts for the 96 oxygen atoms of the 2 × 2 × 1 cell of $La_3Li_3W_2O_{12}$ within the three lowest energy structures **C1**, **C2** and **C3** ($OLaLi_3$, $OLa_2Li_2$, $OLa_3Li$ and $OLa_4$ oxygen environments are given in yellow, purple, cyan and orange, respectively). The calculated $^{17}$O shifts appear to be weakly correlated with the number of $La^{3+}$ ions around a single $O^{2-}$ ion (see Figure S9). Asterisks (*) denote spinning sidebands. (c) $^{17}$O 2D *z*-filtered 3QMAS spectrum of $La_3Li_3W_2{}^{17}O_{12}$ recorded at 9.4 T and under MAS at 13 kHz. The diagonal dotted line represents the isotropic correlation line. Left: isotropic projection of the 2D 3QMAS data. Top: $^{17}$O Hahn echo NMR spectra of $La_3Li_3W_2{}^{17}O_{12}$.

is consistent with the assignment of the peaks at 0.0 and −0.4 ppm as A-site Li ($LiO_4$) and B-site ($LiO_6$) environments.

*3.4.2. $^{17}$O NMR Spectroscopy.* The $^{17}$O Hahn echo spectra obtained for $La_3Li_3W_2{}^{17}O_{12}$ at 9.4 and 20 T show a pattern consisting of multiple overlapping peaks spanning 300 to 500 ppm (Figure 7b). Both spectra have similar line widths and no further line narrowing is seen at high field, as expected for ionic solids.[72] No further spectral resolution is obtained in the 2D 3QMAS NMR spectrum obtained at 9.4 T (Figure 7c) which shows signal along the isotropic diagonal and is indicative of a large distribution of chemical shifts which can be associated with structural disorder.

The accuracy of the calculation of NMR parameters using the GIPAW[38,39] approach has greatly increased and the method can be used with confidence as a predictive tool for spectral assignments of oxide materials.[71,73] GIPAW calculations were used to determine the expected experimental shifts arising from the various local oxygen environments $OLi_3La$, $OLa_2Li_2$, $OLa_3Li$ and $OLa_4$ in $La_3Li_3W_2O_{12}$. Calculated $^{17}$O shifts $\delta$ are distributed over the 300−480 ppm range (Figure 7b) and agree well with the experiment shifts observed in $La_3Li_3W_2{}^{17}O_{12}$. Note that the quadrupolar interaction contribution to the shifts is negligible as evidenced by the absence of field dependence of the $^{17}$O NMR spectra and confirmed by the small calculated quadrupolar induced shift of <10 ppm, as expected for ionic solids (see SI).[72] There is a weak correlation between the predicted shifts and the different number of A-site $Li^+$ ions coordinated to a single $O^{2-}$ ion, the higher shift obtained corresponding to the larger number of coordinated $Li^+$ ions (Figure S9). This trend is expected due to the smaller chemical shieldings (and hence larger shifts) created around oxygens by the smaller four-coordinated $Li^+$ than $La^{3+}$ (ionic radii of 0.76 and 1.03 Å, respectively).[74]

*3.4.3. $Li^+$ Ion Mobility: $^7$Li Line Shape Analysis.* Information on the $Li^+$ ion dynamics was initially obtained from motional narrowing of the static $^6$Li and $^7$Li NMR spectra as a function of temperature. The variable temperature $^7$Li NMR spectra of $La_3Li_3W_2O_{12}$ and $^6$Li NMR spectra of fully $^6$Li enriched $La_3Li_3W_2O_{12}$ ($La_3{}^6Li_3W_2O_{12}$) obtained at 9.4 T are shown in Figure 8. Below room temperature, the $^7$Li static NMR spectra show the anticipated line shape expected for a spin 3/2 nucleus with a dipolar broadened central line (full width at half-maximum of ∼4 kHz) at around 0 ppm corresponding to the +1/2↔−1/2 central transition, and a very broad resonance spanning ∼300 ppm (∼50 kHz) corresponding to the 3/2↔1/2 and −1/2↔−3/2 satellite transitions. The broadening of the central transition is due to the strong $^7$Li−$^7$Li homonuclear dipolar interaction and is averaged out as the temperature is increased due to greater $Li^+$ ion mobility (Figure 8c), yielding motional narrowing of NMR line widths. Similarly, the $^6$Li static NMR lines of $La_3{}^6Li_3W_2O_{12}$ are slightly broadened (∼1.4 kHz) below room temperature and narrow with increasing temperature to ∼0.7 kHz at ∼600 K and ∼0.5 kHz above ∼900 K. The onset of motional narrowing occurs at ∼300 K for both $^6$Li and $^7$Li. At the inflection point of the temperature dependent line narrowing experiment, the $Li^+$ jump rates $\tau^{-1}$ are estimated from the NMR line width in the low temperature rigid-lattice regime $\Delta\omega_{\text{rigid lattice}}$, and yield values of $\sim 9 \times 10^3$ $s^{-1}$ and $\sim 3 \times 10^4$ $s^{-1}$ at 400 and 420 K from $^6$Li and $^7$Li data, respectively.


DOI: 10.1021/acs.chemmater.6b03220
Chem. Mater. XXXX, XXX, XXX−XXX

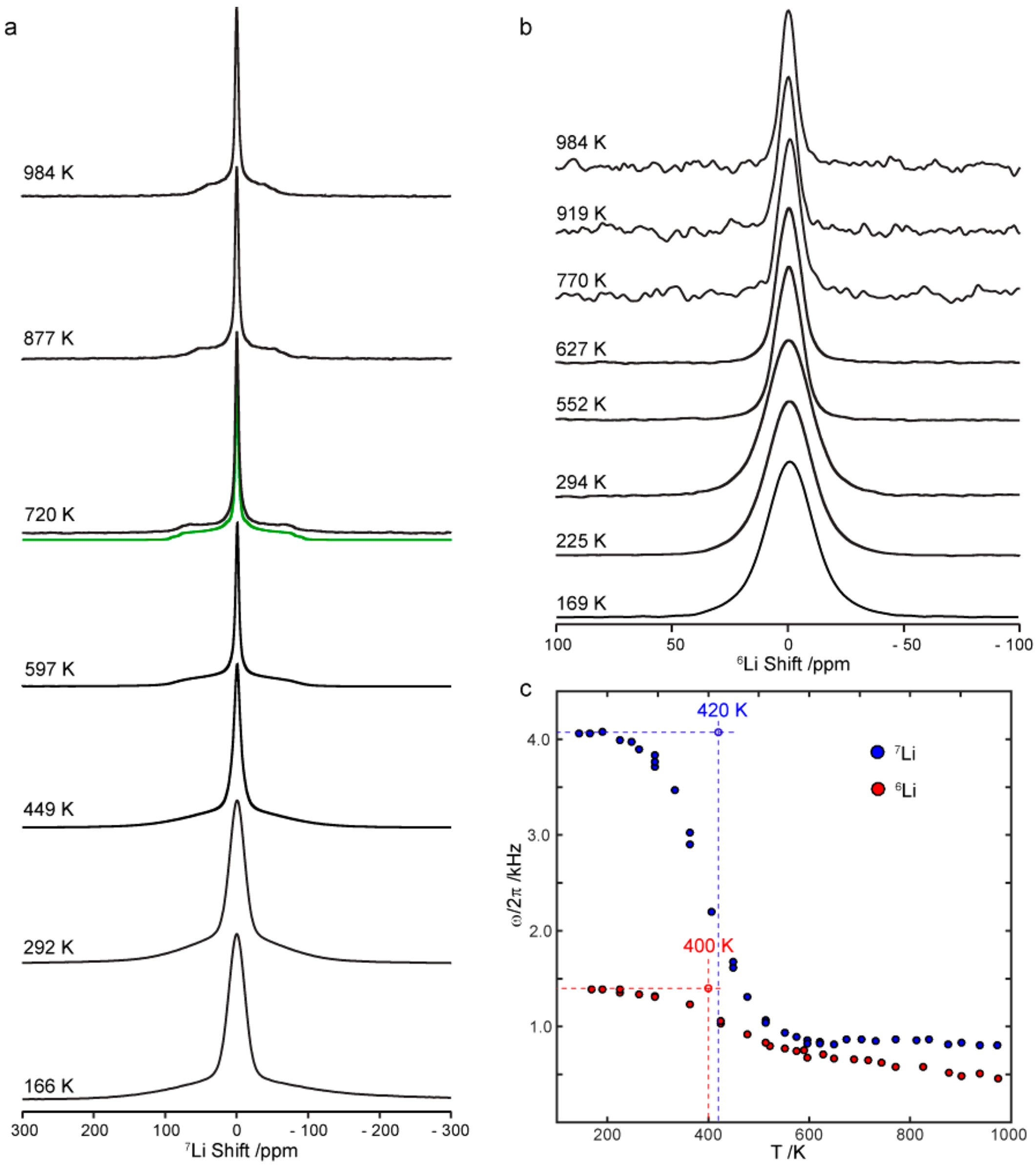


**Figure 8.** $Li^+$ dynamics obtained from NMR motional narrowing. (a) $^7$Li static NMR spectra of $La_3Li_3W_2O_{12}$ and (b) $^6$Li static NMR spectra of $La_3{}^6Li_3W_2O_{12}$ as a function of temperature. The green spectrum in panel a corresponds to a line shape simulation. (c) Temperature dependence of the $^6$Li (red) and $^7$Li (blue) NMR line widths of $La_3Li_3W_2O_{12}$. The vertical and horizontal dashed lines give the temperatures corresponding to the inflection point of the $^{6,7}$Li line narrowing experiments and the rigid-lattice line width $\Delta\omega_{\text{rigid lattice}}$ used to determine the Li jump rates $\tau^{-1}$ ($\tau^{-1} \approx \Delta\omega_{\text{rigid lattice}}$), respectively, and are guides to the eyes.

In the fast motional regime above 420 K, the static $^7$Li NMR spectra show motionally narrowed NMR lines and the typical broad powder pattern line shape characteristics of a spin 3/2 nucleus with the clear discontinuities associated with the satellite transitions. At 720 K, these singularities are observed at ∼−100 and +100 ppm (Figure 8a) from which a quadrupolar coupling constant $C_Q$ of 30 kHz can be estimated. As the temperature is increased to 984 K, the broad static pattern gradually narrows through a continuous averaging of the electric quadrupolar interactions by $Li^+$ ion motion. It is potentially expected that at higher temperature the satellite transitions would completely narrow and vanish due to increasing $Li^+$ ion mobility. However, this regime is not obtained here due to the decomposition of $La_3Li_3W_2O_{12}$, or its reaction with the BN crucible, above 1000 K under the reducing $N_2$/Ar atmosphere of the high temperature laser heated NMR probe used (see Figure S11 for stability test of $La_3Li_3W_2O_{12}$ monitored by PXRD).

*3.4.4. $Li^+$ Ion Mobility: $^{6,7}$Li Spin−Lattice Relaxation Rates.* Figure 9a shows the temperature dependence of the $^6$Li and $^7$Li spin−lattice relaxation rates in the laboratory and rotating frames, $T_1^{-1}$ and $T_{1\rho}^{-1}$, providing $Li^+$ ion dynamics with frequencies on the order of the Larmor ($\nu_0$ = 59 and 156 MHz for $^6$Li and $^7$Li) and spin-lock frequencies ($\nu_1$ = 8 and 14 kHz), respectively, and resulting from fluctuations of the local magnetic dipolar or electrical quadrupolar interactions induced by $Li^+$ ion motion. At temperature below 250 K, the $T_1^{-1}$ and $T_{1\rho}^{-1}$ values are relatively constant, showing little $Li^+$ ion motion. As the temperature is increased to 260 K, the $T_1^{-1}$ and $T_{1\rho}^{-1}$ rates measured for both $^6$Li and $^7$Li become longer and are indicative of a slow motional regime (where $2\pi\nu_0\tau_c$ and $2\pi\nu_1\tau_c \gg 1$ with $\tau_c$ the correlation time of the motion). Here,


DOI: 10.1021/acs.chemmater.6b03220
Chem. Mater. XXXX, XXX, XXX−XXX

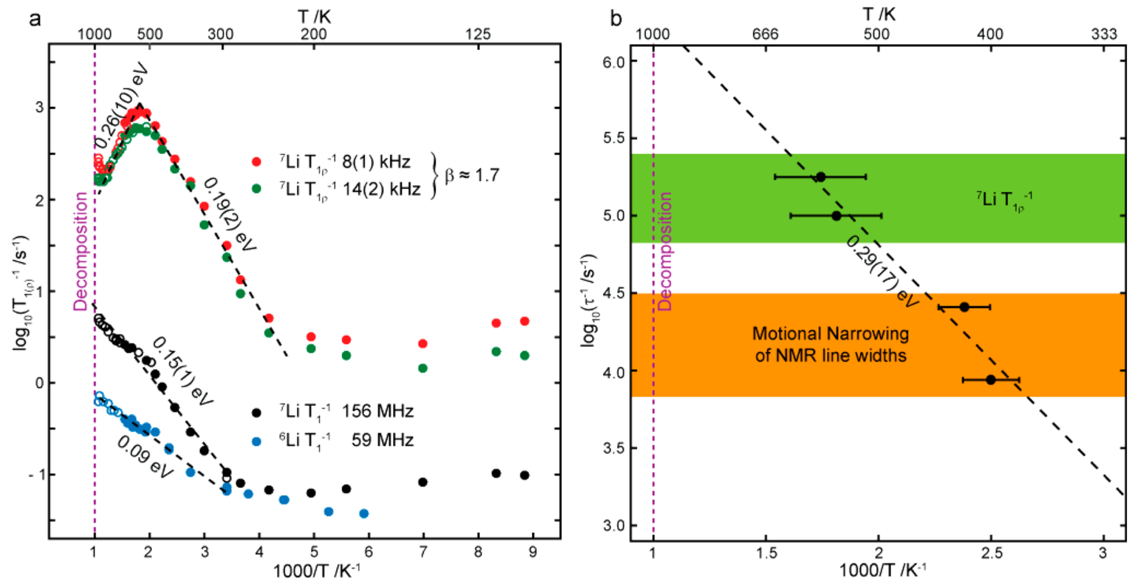


**Figure 9.** $Li^+$ ion dynamics obtained from NMR relaxometry. (a) Arrhenius plot of the spin−lattice relaxation rates $T_1^{-1}$ obtained at $\nu_0(^6Li)$ = 59 MHz (blue) on $La_3{}^6Li_3W_2O_{12}$ and $\nu_0(^7Li)$ = 156 MHz (black), and the spin−lattice relaxation rates in the rotating frame $T_{1\rho}^{-1}$ obtained at $\nu_1(^7Li)$ = 8 kHz (red) and 14 kHz (green) on $La_3Li_3W_2O_{12}$. Filled and empty black circles refer to data obtained with the MAS probes and the laser heated static probe, respectively. The slight anomaly seen at ∼600 K for $^7Li$ $T_1^{-1}$ data perhaps results from the change in NMR probe used to perform the experiment. Dashed lines represent the range where the activation energies $E_a$ and the deviation from BPP theory defined by $\beta$ (see text) are determined. (b) Arrhenius plot of Li jump rates $\tau^{-1}$ extracted from motional narrowing of NMR line width (Figure 8) and the NMR relaxometry data. Horizontal error bars represent the estimated errors of temperature gradient and peak position of $T_{1\rho}^{-1}$ maximum. Vertical error bars are within the size of the symbols. Note that at around 800 K, $T_{1\rho}^{-1}$ minima are seen and may correspond to a different $Li^+$ dynamics mechanism, which is not quantitatively accessible due to sample decomposition at the higher temperatures where data would be needed to probe fully these processes (see Figure S11).

both $T_1^{-1}$ and $T_{1\rho}^{-1}$ rates do not characterize $Li^+$ ion translational diffusion[75] but probe local processes such as hopping between local energy minima that contribute to unsuccessful jumps between cages. Activation energies $E_a$ on the order of 0.09−0.19(2) eV are extracted and are similar to those seen in this regime in other $Li^+$ ion conducting oxides such as $La_{2/3-x}Li_{3x}TiO_3$ $(0.08 < x < 0.167)$[8,76,77] and cubic $Li_7La_3Zr_2O_{12}$.[66]

As the temperature is increased further, $T_{1\rho}^{-1}$ maxima are observed at around 550 K and the $Li^+$ ion jump rates $\tau^{-1}$ are on the order of the spin-lock frequency $\nu_1$ $(2\pi\nu_1\tau \approx 0.5)$[78] yielding values of $1 \times 10^5$ and $1.8 \times 10^5$ $s^{-1}$ at 552 and 574 K. At temperatures above these maxima, the $T_1^{-1}$ and $T_{1\rho}^{-1}$ rates decrease (i.e., the material enters the fast motional regime, $2\pi\nu_0\tau_c$ and $2\pi\nu_1\tau_c \ll 1$) and the jump rates $\tau^{-1}$ relate to $Li^+$ translational diffusion.[79,80] An activation energy of 0.26 ± 0.10 eV is determined from the $^7Li$ $T_{1\rho}^{-1}$ relaxation rates in this regime. The frequency dependence of $T_1^{-1}$ and $T_{1\rho}^{-1}$ rates in the fast motional regime ($2\pi\nu_0\tau$ and $2\pi\nu_1\tau \ll 1$) is well-known to relate to the dimensionality of the diffusion processes.[65,79] Figure 9a shows that the $^7Li$ $T_{1\rho}^{-1}$ rates obtained over the 600−800 K temperature range and probed at two different spin lock frequencies ($\nu_1$ = 8 and 14 kHz) are independent of frequency. This is characteristic of 3D diffusion of $Li^+$ ions in $La_3Li_3W_2O_{12}$.

The asymmetric behavior of the temperature dependence of the $T_{1\rho}^{-1}$ rates on either side of the maxima has been well documented in the literature for fast ion conductors and disordered materials, and arises from a combination of structural disorder and Coulombic interactions of mobile ions.[62,79] This yields a deviation from the Bloembergen−Purcell−Pound (BPP)[81] theory of relaxation (which predicts symmetric peaks and a quadratic frequency dependence of the relaxation rates $T_{1\rho}^{-1} \propto \nu^{-2}$) giving in the slow motional regime $(2\pi\nu_1\tau \gg 1)$ a frequency dependence of the form $T_{1\rho}^{-1} \propto \nu^{-\beta}$, where the model parameter $\beta$ ranges between 1 and 2. Our data in the two low temperature flanks of the $T_{1\rho}^{-1}$ rates are indeed frequency-dependent and fit to an exponent $\beta$ = 1.7 for $^7Li$ $T_{1\rho}^{-1}$ (using the equation $E_{a,low} = (\beta - 1)E_{a,high}$[79] where $E_{a,low}$ = 0.19 eV and $E_{a,high}$ = 0.26 eV are the activation energies on the low and high temperature flanks, respectively). The higher activation energy observed at high temperature accounts for cooperative effects such as long-range Coulombic interactions between charge carriers or structural disorder that produce multiple or correlated hops over longer distances than probed in the lower temperature regime, and corresponds to translational diffusion of $Li^+$ ions.[78]

The jump rates $\tau^{-1}$ extracted from the NMR relaxometry data (that is the two maxima of the $^7Li$ $T_{1\rho}^{-1}$ data, Figure 9a) and the line narrowing experiments (Figure 8c) are plotted against reciprocal temperature (Figure 9b). The fit to the data using an Arrhenius equation of the form $\tau^{-1} = \tau_0^{-1}\exp(E_a/RT)$ is reasonably good and yields an activation energy $E_a$ of 0.29 ± 0.17 eV and a prefactor $\tau_0^{-1}$ of ∼6 × $10^7$ $s^{-1}$. The activation energy determined here is identical to the value seen in the high temperature flank of the $^7Li$ spin−lattice relaxation rate plot (Figure 9a) within experimental error, which suggests that we probe the same diffusive process in both line narrowing and relaxometry experiments.

An NMR conductivity $\sigma_{NMR}$ can be calculated from this NMR-derived $Li^+$ ion jump rate $\tau^{-1}$ (Figure 9b) by combining the Nernst−Einstein and the Einstein−Smoluchowski equations to give the following expression:


DOI: 10.1021/acs.chemmater.6b03220
Chem. Mater. XXXX, XXX, XXX−XXX

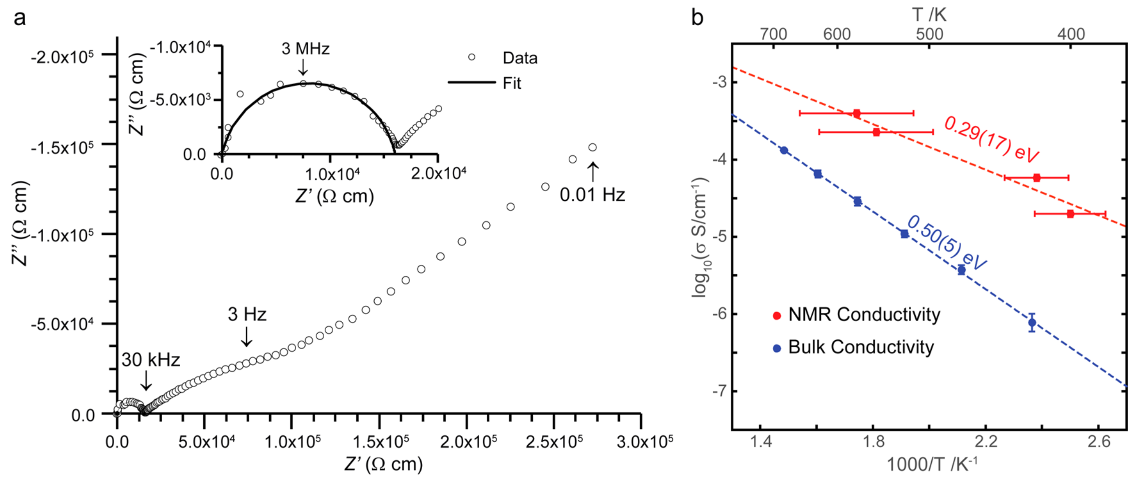


**Figure 10.** AC impedance data of $La_3Li_3W_2O_{12}$. (a) Complex impedance plot at 350 °C in air along with the fitting of the bulk arc with an equivalent circuit of resistor-constant phase element (inset). (b) Bulk conductivities $\sigma$ of $La_3Li_3W_2O_{12}$ vs temperature obtained from the AC impedance data, and extracted from the NMR $Li^+$ jump rates $\tau^{-1}$ obtained from $^7Li$ relaxation rates $T_{1\rho}^{-1}$ and motional narrowing using the Nernst–Einstein–Smoluchowski equations. The horizontal error bar on the NMR conductivity is an estimation of the temperature gradient on NMR probe and the peak position for $T_{1\rho}^{-1}$ maximum.

$$\sigma_{NMR} = \frac{f}{H_R}\frac{Nq^2a^2}{6k_BT}\frac{1}{\tau}$$

where $f/H_R$ is the ratio of the correlation factor and Haven ratio (set to 1 for uncorrelated motion), $N$ is the number of charge carriers (assumed as 1 A-site Li) per unit cell volume (245 Å$^3$), $q$ is the ionic charge of $Li^+$ and a is the average jump distance (taken as 4 ± 0.2 Å for A-site Li–Li distance, see Figure S4), and yields values in the range of $5.8 \times 10^{-5} - 2.2 \times 10^{-4}$ S/cm between 400 and 574 K (Figure 10b).

**3.5. AC Impedance Spectroscopy.** Dilatometry measurements were peformed to determine the optimal sintering conditions (Figure S12). No abrupt jump was observed between 50 and 860 °C which suggests that no phase transition occurs in this temperature range. The data show that densification starts at 400 °C and has almost ceased after 24 h at 860 °C. Consequently, pellets were formed by sintering for 36 h at 900 °C and used for AC impedance spectroscopy measurements.

The preliminary impedance data collected under both dry and wet air showed no significant difference, thus showing no evidence of proton conductivity and subsequent measurements were performed in ambient air. The typical complex impedance data for $La_3Li_3W_2O_{12}$ with a density of 67% is shown in Figure 10a. Data fitting using the ZView software package shows the high frequency semicircle has an associated capacitance of 2.6 pF/cm (corresponding to a relative permittivity of 29) and is therefore assigned to the bulk response. The suppressed arc at intermediate frequency 3 Hz–30 kHz and the low frequency spike are attributed to the electrode response. The low frequency spike at 0.01 Hz is characteristic of the known Warburg impedance associated with Li ion diffusion in the electrode and indicates negligible electronic conduction. Note that the capacitance associated with the arc at 3 Hz–30 kHz is of the order of $10^{-6}$ F/cm that is too large for a grain boundary response but matches well with an electrode response.[82] No separate arc associated with the grain boundary response is observed, suggesting the sample is electrically homogeneous. The low density of the sample indicates incomplete ceramic sintering, which may lead to the same electrical response from grain and grain boundary regions, e.g., because there are no compositional changes. The grain boundary arc may also be completely masked by the large electrode arc at 3 Hz–30 kHz. Thus, only bulk conductivity was extracted from the data. The conductivity of $La_3Li_3W_2O_{12}$ as a function of temperature (150–400 °C) is shown in Figure 10b. A bulk conductivity at 400 °C of $1.32(3) \times 10^{-4}$ S/cm is obtained, which is much lower than those obtained for the LLTO family ($\sigma_{bulk} \approx 10^{-3}$ S/cm at room temperature for $x = 0.1$).[83] Arrhenius fits to the conductivities yield an activation energy of 0.50 ± 0.05 eV, which is greater than the typical activation energy obtained for the LLTO family (between 0.35–0.4 eV).[83]

## 4. DISCUSSION

The structure of $La_3Li_3W_2O_{12}$ differs from those of $La_{2/3-x}Li_{3x}TiO_3$ in several key respects: these are A-site cation ordering, B-site cation ordering and octahedral tilting of the $BO_6$ framework. LLTO structures show a strong tendency toward layered ordering of $Li^+$ and $La^{3+}$ cations, which stack in alternating two-dimensional La-rich and La-poor layers, with a degree of ordering that is dependent on thermal history and precise composition.[84] In contrast, the A-site cations in $La_3Li_3W_2O_{12}$ are distributed uniformly in three dimensions. The B-site cations in $La_3Li_3W_2O_{12}$ are fully ordered in a rock salt arrangement, so that each A-site is delimited by four $WO_6$ octahedra and four $LiO_6$ octahedra. The framework is distorted by two out-of-phase octahedral tilts of equal magnitude and one in-phase tilt described by the tilt scheme $b^-b^-c^+$: the resulting Li–O–W bond angles lie in the range 152.5(1)°–153.3(1)°, which are similar in magnitude to those exhibited by other perovskites with this tilt scheme, such as the single perovskite orthoferrites[85] and the Li containing double perovskite $La_2LiSbO_6$.[27,86] These tilts are larger than those reported in the $La_{2/3-x}Li_{3x}TiO_3$ family of compounds, which host a smaller B-site cation ($r$ = 0.605 Å for $Ti^{4+}$, versus 0.76 and 0.60 Å for $Li^+$ and $W^{6+}$ respectively).[74] For example, $La_{0.567}Li_{0.3}TiO_3$ and $La_{0.62}Li_{0.16}TiO_3$ each exhibit only a single out-of-phase octahedral tilt with minimum Ti–O–Ti angles of 168.1(3)°[87] and 168.9(3)°,[57] respectively, whereas the most La-deficient


DOI: 10.1021/acs.chemmater.6b03220
Chem. Mater. XXXX, XXX, XXX–XXX

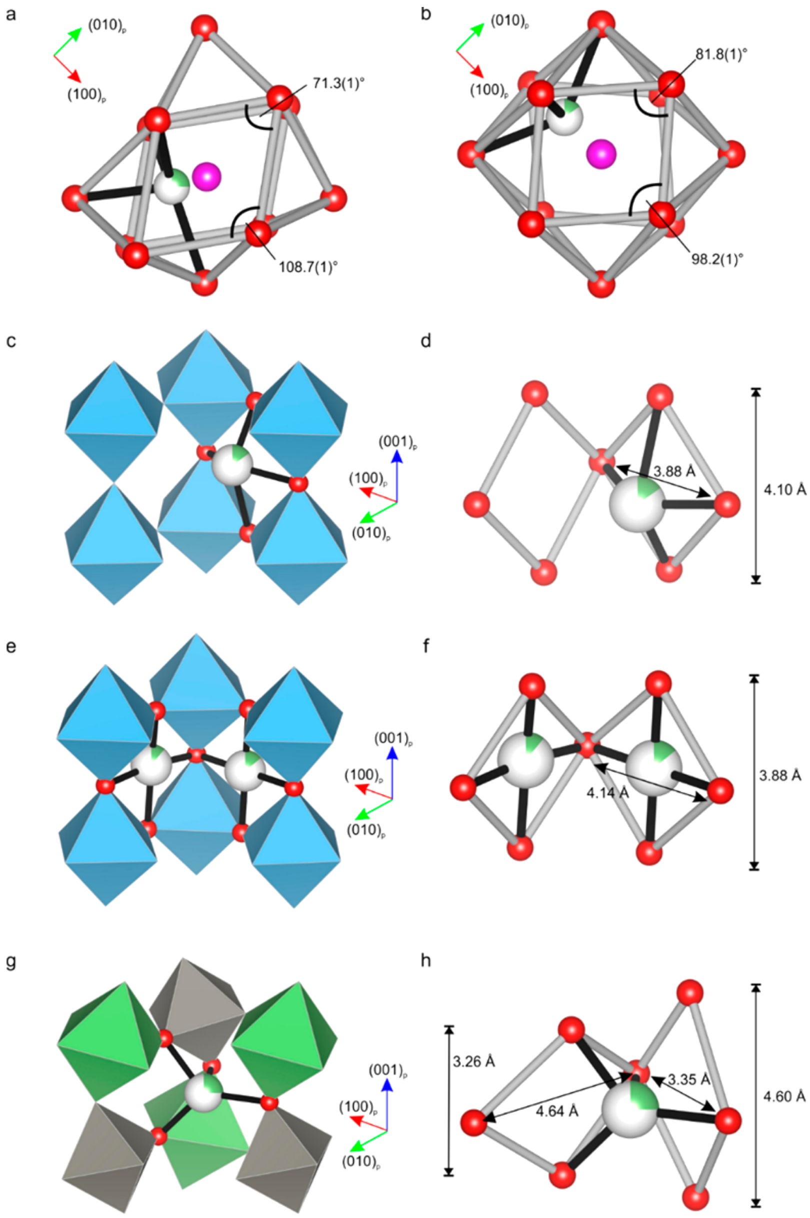


**Figure 11.** Comparison of the local coordination environments of $Li^+$ at the A-sites of $La_3Li_3W_2O_{12}$ (from PND at 5 K) and $Li_{2/3-x}Li_{3x}TiO_3$. (a) The distorted $LiO_{12}$ cuboctahedron in $La_3Li_3W_2O_{12}$, showing the displacement of $Li^+$ (green atom) from the $O_{12}$ centroid (magenta atom) approximately along the $(110)_p$ direction toward the vertices of two adjoining $BO_6$ octahedra, and (b) the near-regular $LiO_{12}$ cuboctahedra in tetragonal $Li_{0.563}Li_{0.3}TiO_3$[84] where $Li^+$ is displaced from the $O_{12}$ centroid toward the square windows, shown here along $(100)_p$. (c and d) The 4-fold coordination of Li in tetragonal $La_{0.563}Li_{0.3}TiO_3$[84] is formed by four oxides from the same window, and Li is displaced from the plane of the window toward the center of the $O_{12}$ cuboctahedron. (e and f) The 4-fold coordination of Li in rhombohedral $Li_{0.5}Li_{0.5}TiO_3$,[88] where Li lies in the planes of the windows. (g and h) The distorted tetrahedral site occupied by Li in $La_3Li_3W_2O_{12}$ is formed by oxide ions from two adjoining windows due to the distortion of the planar window site by the octahedral tilting. Green octahedra are $LiO_6$, gray octahedra are $WO_6$, blue octahedra are $TiO_6$, red atoms are oxide ions.

member of the series $La_{0.5}Li_{0.5}TiO_3$ exhibits three equivalent out of phase tilts with a Ti−O−Ti angle of 169.6(3)°.[88]

The nature of the tilts influences the shape of the windows connecting adjacent A-sites. In the $La_{2/3-x}Li_{3x}TiO_3$ system, the relatively weak tilts subject the windows in the $O_{12}$ cages to a small rhombic distortion away from their ideal square geometry in the cubic perovskite structure. For example, in $La_{0.567}Li_{0.3}TiO_3$ the internal angles of the most distorted window are 81.8(1)°/98.2(1)°,[87] whereas in $La_3Li_3W_2O_{12}$ the octahedral tilts impose a far stronger rhombic distortion on the windows, producing internal angles of 71.4(1)°/108.6(1)° (Figure 11a,b). The B-site rock salt ordering of Li and W in $La_3Li_3W_2O_{12}$ has further implications for the distortion of the window sites, because although the individual $LiO_6$ and $WO_6$ octahedra in $La_3Li_3W_2O_{12}$ are both highly regular (their bond length distortion indices[89,90] are 0.0018 and 0.0015 respectively, and their bond angle variances[89,91] are 0.328 and 0.309 respectively; these values closely match the range of values exhibited by $CaTiO_3$[92]), there is a considerable size mismatch between them (the respective octahedral volumes are 12.9 and 9.3 Å$^3$ for $LiO_6$ and $WO_6$). This size difference between the two B-sites introduces two distinct edge lengths to the windows which distorts the rhombus (produced by octahedral tilting only) to a parallelogram. Despite the large distortion, the


DOI: 10.1021/acs.chemmater.6b03220
Chem. Mater. XXXX, XXX, XXX−XXX

windows of $La_3Li_3W_2O_{12}$ have a greater area than those of $La_{0.567}Li_{0.3}TiO_3$ (8.0 and 7.1 Å$^2$, respectively) because of the large size of the B-site $LiO_6$ unit.

The nature of this distortion of the windows underpins the difference in the local coordination environment of A-site Li between $La_3Li_3W_2O_{12}$ and $La_{2/3-x}Li_{3x}TiO_3$. In $La_{2/3-x}Li_{3x}TiO_3$, Li is always coordinated to the four oxide ions that define the window, as it occupies either the square planar site at the center of the windows (in $La_{0.62}Li_{0.16}TiO_3$ and $La_{0.5}Li_{0.5}TiO_3$[57,88]) or is subject to a small displacement from this site along the $[100]_p$ direction (in $La_{0.567}Li_{0.3}TiO_3$[52,87]), because the near-regular geometry of these sites (small rhombic distortion and regular edge length, producing two diagonals of approximately 4 Å) means that four favorable Li−O distances (of approximately 2 Å) can be obtained simultaneously by occupying them (Figure 11c−f). The center of the $O_{12}$ cage corresponds to an energy maximum for Li in the LLTO family because it would be considerably under-bonded there. In contrast, these sites are not occupied in $La_3Li_3W_2O_{12}$, where the highly distorted windows have diagonals of 3.3 and 4.6 Å (Figure 11g,h). This precludes the coordination of Li by four oxides from a single window, which would either generate two unphysically short Li−O distances (in the case where Li lies in the plane of the window) or two unphysically long Li−O distances (in the case where Li is displaced from the window along $[100]_p$). Instead, 4-fold coordination of Li is achieved by occupying a distorted tetrahedral site, which is defined by the short diagonals of two adjacent windows, with Li displaced from the centroid of the $O_{12}$ cage along $[110]_p$ (Figure 11g). This site has no equivalent in the $La_{2/3-x}Li_{3x}TiO_3$ structures (Figure 11h), as it is a product of the $b^-b^-c^+$ octahedral tilting. Octahedral tilting and the distortion enforced on the window sites by the B-site alternation between Li and W prevents Li from occupying the sites in the window between the cages, and an appropriate alternative coordination for Li is found within the cage. The resulting A-site Li−O distances lie in the range 2.11(2)−2.20(2) Å with tetrahedral angles in the range 78.4(3)°−131.4(6)° at 5 K.

The site percolation threshold for a simple cubic lattice is 0.31. For an A-site sublattice containing randomly placed 0.25 $Li^+$ ions, we would therefore not expect a percolating pathway of $Li^+$ ions throughout the structure, thus limiting the ionic conductivity of such a system, because transport of $Li^+$ ions through an A-site occupied by an $La^{3+}$ ion is likely to be difficult. Conductivity is strongly suppressed below the site percolation threshold in LLTO and related materials,[93] and this combination of A-site blocking by $La^{3+}$ and the absence of Li vacancies in the nominal composition (vacancies are possible within experimental uncertainty) explain the lower NMR and impedance conductivities measured for $La_3Li_3W_2O_{12}$ than the LLTO family: for example, motional narrowing of the Li NMR occurs at a higher temperature than that observed for $La_{2/3-x}Li_{3x}TiO_3$ (∼170 K for $x$ = 0.06)[94,95] and doped $Li_7La_3Zr_2O_{12}$ (<170 K).[66] Local ordering of the $Li^+$ ions, as observed computationally in section 3.3.2, could overcome the percolation problem to some extent by removing some of the randomness that underpins the threshold calculation, forming layers within $La_3Li_3W_2O_{12}$ with a higher concentration of $Li^+$ ions. The presence of $Li^+$ ions on the perovskite B-site opens another pathway to overcome this barrier to long-range diffusion, as long as site exchange between the A- and B-sites is possible. AIMD calculations (section 3.3.4) suggest that this is indeed the case in $La_3Li_3W_2O_{12}$.

The computed energy landscape for $Li^+$ ions within $La_3Li_3W_2O_{12}$ is considerably more complicated than that of $La_{2/3-x}Li_{3x}TiO_3$.[96] There are multiple local energy minima for A-site $Li^+$ ions in $La_3Li_3W_2O_{12}$ (Figure 4), resulting in an $O_{12}$ cage to $O_{12}$ cage pathway involving multiple events, each with different barriers (Figure 6). $Li^+$ ions in $La_{2/3-x}Li_{3x}TiO_3$ are proposed to move via single hops of around 4 Å from one window site to the next,[96] whereas in $La_3Li_3W_2O_{12}$ single hops take place on the 1.5−2.5 Å length scale (Figure 6), with an energy maximum rather than an energy minimum at the window site. It is likely that $Li^+$ ion transport in $La_3Li_3W_2O_{12}$ is best described by a large number of small hopping events with energy barriers of 0.1−0.25 eV, each with differing energy barriers, some of which involve $Li^+$ ion motion within an $O_{12}$ cage, and others $O_{12}$ cage to neighboring $O_{12}$ cage motion: this 3D diffusion is verified experimentally with the measurements of frequency independent relaxation rates. This mechanism of transport is more closely related to those proposed for the $Li^+$ ion conducting $Li_7La_3Zr_2O_{12}$ based garnets[97] and the $LiTi_2(PO_4)_3$ based NASICON systems[98] than the proposed transport pathways in the perovskite $La_{2/3-x}Li_{3x}TiO_3$, to which $La_3Li_3W_2O_{12}$ appears more closely related structurally. The different pathways in the two perovskites can be traced to the influence of the distortion of the originally square windows by the B-site Li in $La_3Li_3W_2O_{12}$ that displaces A-site Li nearer to the cage center and drives octahedral tilting to form the tetrahedral coordination.

DFT barriers between the possible $Li^+$ ion locations within a single $O_{12}$ cage are less than 0.1 eV (section 3.3.1), and AIMD calculations (Figure 4) suggest that hopping between the sites available to Li within a single $O_{12}$ cage occurs with frequencies of $10^{11}$−$10^{12}$ Hz at room temperature. This is faster than the frequencies probed by NMR line narrowing ($10^3$ Hz) and relaxometry experiments ($10^9$ Hz), and AC impedance spectroscopy ($10^7$ Hz), suggesting that these experiments instead probe rarer hopping events between $O_{12}$ cages which occur at a lower frequency. The computed barriers of 0.11−0.14 eV for single hopping events involving Li passing through the window between two $O_{12}$ cages (labeled 1 and 5 in Figures 6 and S7), are in good agreement to the activation energies of 0.09−0.19 ± 0.02 eV extracted from the low temperature flanks of NMR spin−lattice relaxation rates $T_1^{-1}$ and $T_{1\rho}^{-1}$ data, which reflect single hopping events including unsuccessful jumps within $La_3Li_3W_2O_{12}$.

The activation energy extracted from the high temperature flank of the $T_{1\rho}^{-1}$ relaxation data (0.26 ± 0.10 eV) and from the jump rates obtained the $^{6,7}$Li line narrowing experiments and the $T_{1\rho}^{-1}$ maxima (0.29 ± 0.17 eV) are identical within experimental error, and reflect the barrier to the same 3D translational diffusion process. These values are similar to the maximum energy barrier calculated for the $O_{12}$ cage to neighboring $O_{12}$ cage pathway (Figure 6e) and suggest that we probe this diffusive process, which can involve multiple hops because of the multiple minima on the path. The activation energy obtained on the high temperature flank (0.26 eV) of the $T_{1\rho}^{-1}$ data is similar to those of $La_{2/3-x}Li_{3x}TiO_3$ (0.20 eV for $x$ = 0.11,[8] 0.26 eV for $x$ = 0.08,[76] and 0.26 eV for $x$ = 0.167)[77] and doped $Li_7La_3Zr_2O_{12}$ (0.34 eV)[66] which suggests that barrier to $O_{12}$ cage to $O_{12}$ cage $Li^+$ ion diffusion in $La_3Li_3W_2O_{12}$ probed by NMR is comparable to the best oxide $Li^+$ ion conductors reported, despite the considerable structural and $Li^+$ diffusive pathway differences from the LLTO family.[7−9] In this phase, the relaxometry plot for $Li^+$ ions in $La_{2/3-x}Li_{3x}TiO_3$ ($x$ =


DOI: 10.1021/acs.chemmater.6b03220
Chem. Mater. XXXX, XXX, XXX−XXX

0.11) shows two motional regimes: at low temperatures ($T$ < 200 K) a 2D diffusion process is observed, where only the bottlenecks between $O_{12}$ cages on the same $La^{3+}$ poor layers are large enough to accommodate $Li^+$ ion transport in the material, and a 3D diffusion process above 200 K, where thermal agitation opens up the bottleneck between $La^{3+}$ rich and $La^{3+}$ poor layers allowing $Li^+$ to hop between the two layers.[7−9]

The prefactor $\tau_0^{-1}$ in the Arrhenius fit is lower than seen in $La_{2/3-x}Li_{3x}TiO_3$ ($x$ = 0.08, $\tau_0^{-1} = 4.6 \times 10^{11}$ s$^{-1}$),[76] and some other fast Li conductors[99−101] but comparable to $Li_2Ti_3O_7$ ($\tau_0^{-1} = 2.5 \times 10^8$ s$^{-1}$).[102] It is below single phonon frequencies in the material and more consistent with a small, temperature-independent contribution to the success of an individual hop, as might arise from a low defect concentration of charge carrying Li vacancy defects, than a single attempt frequency.

The activation energy for $Li^+$ site-to-site motion obtained from NMR conductivity (0.29 ± 0.17 eV) is smaller than the value determined through impedance measurements (0.50 ± 0.05 eV), such a discrepancy is not uncommon in the literature of fast ion conductors,[69,99,103−105] including $La_{2/3-x}Li_{3x}TiO_3$,[76,106] and has been discussed extensively before.[107] The activation energy obtained from the $^{6,7}Li$ NMR data set can be assigned to migration between $O_{12}$ cages, whereas that obtained from conductivity is often larger as it may contain additional contributions such as defect formation, and defect association that are involved in longer-range transport of Li between multiple cages: the barriers posed to this by percolation and the low formal vacancy concentration in $La_3Li_3W_2O_{12}$ are discussed above. Defect creation energies are in the range 0.4−0.6 eV in $La_3Li_3W_2O_{12}$ from the small supercell calculations presented here. The NMR conductivity is higher than the bulk impedance conductivity (by up to 2 orders of magnitude at low temperature (Figure 10b). This discrepancy is observed in other systems,[69,76,101,107,108] as unsuccessful $Li^+$ ion jumps (that is a moving ion returning to its original site rather than hopping further to the next site) contribute to the motional narrowing of the NMR spectra and the relaxation rates without producing longer range $Li^+$ ion transport probed by impedance spectroscopy.[107,109] For example, NMR conductivity is 1 order of magnitude higher than values obtained in impedance spectroscopy for $La_{2/3-x}Li_{3x}TiO_3$ ($x$ = 0.08)[76] and $Li_2ZrO_3$.[108]

## 5. CONCLUSIONS

The presence of Li on both the A- and B-sites in $La_3Li_3W_2O_{12}$ gives it quite different crystal chemistry and Li dynamics from the well-known $La_{2/3-x}Li_{3x}TiO_3$ family that is based on the same perovskite structure. Although $La_3Li_3W_2O_{12}$ contains few vacancies and has a blocked percolation path, the barrier to cage-to-cage mobility of the A-site Li is comparable to those in the best known Li conducting oxides. The pathway between cages is more complex in $La_3Li_3W_2O_{12}$ than in $La_{2/3-x}Li_{3x}TiO_3$, with multiple minima, because of the quite different A-site Li position which is toward the center of the $O_{12}$ cage rather than in its windows. This A-site location is produced by the window distortions that are driven by the difference in size between the Li and W cations occupying the B-site and the tilting required to coordinate the A-site Li. A-site to B-site hops are also now possible, and observed in AIMD simulations of Li motion. Control of the defect chemistry in $La_3Li_3W_2O_{12}$ to increase the carrier concentration and control the A-site to A-site and A-site to B-site pathways thus offers a new route to Li conducting oxides.

## ■ ASSOCIATED CONTENT

### Supporting Information

The Supporting Information is available free of charge on the ACS Publications website at DOI: 10.1021/acs.chemmater.6b03220.

TEM-EDX and ICP-OES data, additional diffraction data and refinement table, local A-site Li coordination environments of DFT calculated structures, additional $^6Li$ MAS NMR spectra and $La_3Li_3W_2O_{12}$ temperature stability test (PDF)

## ■ AUTHOR INFORMATION


### Corresponding Authors

*E-mail: frederic.blanc@liverpool.ac.uk (F.B.).

*E-mail: m.j.rosseinsky@liverpool.ac.uk (M.J.R.).


### Notes

The authors declare no competing financial interest.

## ■ ACKNOWLEDGMENTS


We thank George Miller for ICP-OES measurements, Dr. Claire Murray and Prof. Chiu Tang for assistance on beamline I11 (Diamond, UK), Dr. Kevin Knight and Dr. Dominic Fortes for assistance on HRPD (ISIS, UK) and Dr. Pierre Florian (CEMHTI-CNRS, France) for access to the laser-heated high-temperature static NMR probe and fruitful discussions. We thank EPSRC for funding under EP/H000925 and EP/N004884 and a studentship to K.K.I. F.B. thanks the University of Liverpool and the STFC for funding via an Early Career Award. Computational resources were provided by the University of Liverpool, the N8 HPC Centre of Excellence, provided and funded by the N8 consortium and EPSRC (EP/K000225/1), and the ARCHER UK National Supercomputing Service (http://www.archer.ac.uk) via our membership of the UK's HEC Materials Chemistry Consortium, which is funded by EPSRC (EP/L000202). The UK 850 MHz solid-state NMR Facility used in this research was funded by EPSRC and BBSRC (contract reference PR140003), as well as the University of Warwick including via part funding through Birmingham Science City Advanced Materials Projects 1 and 2 supported by Advantage West Midlands (AWM) and the European Regional Development Fund (ERDF). Collaborative assistance from the 850 MHz Facility Manager (Dr. Dinu Iuga, University of Warwick) is acknowledged. M.J.R. is a Royal Society Research Professor. Original data is also available at the University of Liverpool's DataCat repository at http://datacat.liverpool.ac.uk/id/eprint/162.


## ■ REFERENCES


(1) Bachman, J. C.; Muy, S.; Grimaud, A.; Chang, H.-H.; Pour, N.; Lux, S. F.; Paschos, O.; Maglia, F.; Lupart, S.; Lamp, P.; Giordano, L.; Shao-Horn, Y. Inorganic Solid-State Electrolytes for Lithium Batteries: Mechanisms and Properties Governing Ion Conduction. *Chem. Rev.* **2016**, *116*, 140−162.

(2) Kamaya, N.; Homma, K.; Yamakawa, Y.; Hirayama, M.; Kanno, R.; Yonemura, M.; Kamiyama, T.; Kato, Y.; Hama, S.; Kawamoto, K.; Mitsui, A. A Lithium Superionic Conductor. *Nat. Mater.* **2011**, *10*, 682−686.

(3) Kuhn, A.; Gerbig, O.; Zhu, C.; Falkenberg, F.; Maier, J.; Lotsch, B. V. A New Ultrafast Superionic Li-Conductor: Ion Dynamics in $Li_{11}Si_2PS_{12}$ and Comparison with Other Tetragonal LGPS-Type Electrolytes. *Phys. Chem. Chem. Phys.* **2014**, *16*, 14669−14674.

(4) Muramatsu, H.; Hayashi, A.; Ohtomo, T.; Hama, S.; Tatsumisago, M. Structural Change of $Li_2S$-$P_2S_5$ Sulfide Solid Electrolytes in the Atmosphere. *Solid State Ionics* **2011**, *182*, 116−119.

(5) Aguesse, F.; López del Amo, J. M.; Roddatis, V.; Aguadero, A.; Kilner, J. A. Enhancement of the Grain Boundary Conductivity in Ceramic $Li_{0.34}La_{0.55}TiO_3$ Electrolytes in a Moisture-Free Processing Environment. *Adv. Mater. Interfaces* **2014**, *1*, 910−924.

(6) Bernuy-Lopez, C.; Manalastas, W.; Lopez Del Amo, J. M.; Aguadero, A.; Aguesse, F.; Kilner, J. A. Atmosphere Controlled Processing of Ga-Substituted Garnets for High Li-Ion Conductivity Ceramics. *Chem. Mater.* **2014**, *26*, 3610−3617.

(7) Emery, J.; Bohnké, O.; Fourquet, J. L.; Buzaré, J. Y.; Florian, P.; Massiot, D. Nuclear Magnetic Resonance Investigation of $Li^+$-Ion Dynamics in the Perovskite Fast-Ion Conductor $Li_{3x}La_{2/3-x}\square_{1/3-x}TiO_3$. *J. Phys.: Condens. Matter* **2002**, *14*, 523−539.

(8) Bohnke, O.; Emery, J.; Fourquet, J. L. Anomalies in $Li^+$ Ion Dynamics Observed by Impedance Spectroscopy and $^7$Li NMR in the Perovskite Fast Ion Conductor $(Li_{3x}La_{2/3-x}\square_{1/3-2x})TiO_3$. *Solid State Ionics* **2003**, *158*, 119−132.

(9) Bohnke, O. The Fast Lithium-Ion Conducting Oxides $Li_{3x}La_{2/3-x}TiO_3$ from Fundamentals to Application. *Solid State Ionics* **2008**, *179*, 9−15.

(10) Knauth, P. Inorganic Solid Li Ion Conductors: An Overview. *Solid State Ionics* **2009**, *180*, 911−916.

(11) Belous, A. G.; Gavrilenko, O. N.; Pashkova, E. V.; Danil'chenko, K. P.; V'yunov, O. I. Effect of Synthesis Conditions on the Lithium Nonstoichiometry and Properties of $La_{2/3-x}Li_{3x}\square_{4/3-2x}M_2O_6$ (M = Nb, Ta) Perovskite-like Solid Solutions. *Inorg. Mater.* **2004**, *40*, 867−873.

(12) Yang, K. Y.; Fung, K. Z. Effect of $Li^+$ Addition on Crystal Structure and Electrical Conduction of Highly Defective $La_{1/3}NbO_3$ Perovskite. *J. Phys. Chem. Solids* **2008**, *69*, 393−399.

(13) Arakawa, S.; Shiotsu, T.; Hayashi, S. Non-Arrhenius Temperature Dependence of Conductivity in Lanthanum Lithium Tantalate. *J. Ceram. Soc. Japan* **2005**, *113*, 317−319.

(14) Mizumoto, K.; Hayashi, S. Crystal Structure and Lithium Ion Conductivity of A-Site Deficient Perovskites $La_{1/3-x}Li_{3x}TaO_3$. *Nippon Seramikkusu Kyokai Gakujutsu Ronbunshi* **1997**, *105*, 713−715.

(15) Mizumoto, K.; Hayashi, S. Lithium Ion Conduction in A-Site Deficient Perovskites $R_{1/4}Li_{1/4}TaO_3$ (R = La, Nd, Sm and Y). *Solid State Ionics* **1999**, *116*, 263−269.

(16) Vijayakumar, M.; Emery, J.; Bohnke, O.; Vold, R. L.; Hoatson, G. L. $^7$Li NMR Analysis on Perovskite Structured $Li_{0.15}La_{0.28}TaO_3$. *Solid State Ionics* **2006**, *177*, 1673−1676.

(17) Katsumata, T.; Takahata, M.; Mochizuki, N.; Inaguma, Y. The Relationship between Li Ion Conductivity and Crystal Structure for Ordered Perovskite Compounds, $(La_{2/3-1/3p}Li_p)(Mg_{1/2}W_{1/2})O_3$ ($p$ = 0.05, 0.11 and 0.14). *Solid State Ionics* **2004**, *171*, 191−198.

(18) Chung, H.-T.; Kim, J.-G.; Kim, H.-G. Dependence of the Lithium Ionic Conductivity on the B-Site Ion Substitution in $(Li_{0.5}La_{0.5})Ti_{1-x}M_xO_3$ (M = Sn, Zr, Mn, Ge). *Solid State Ionics* **1998**, *107*, 153−160.

(19) Harada, Y.; Watanabe, H.; Kuwano, J.; Saito, Y. Lithium Ion Conductivity of A-Site Deficient Perovskite Solid Solutions. *J. Power Sources* **1999**, *81−82*, 777−781.

(20) Thangadurai, V.; Shukla, A. K.; Gopalakrishnan, J. $LiSr_{1.65}\square_{0.35}B_{1.3}B'_{1.7}O_9$ (B = Ti, Zr; B′ = Nb, Ta): New Lithium Ion Conductors Based on the Perovskite Structure. *Chem. Mater.* **1999**, *11*, 835−839.

(21) Sebastian, L.; Gopalakrishnan, J. Lithium Ion Mobility in Metal Oxides: A Materials Chemistry Perspective. *J. Mater. Chem.* **2003**, *13*, 433−441.

(22) Borisevich, A. Y.; Davies, P. K. $La(Li_{1/3}Ti_{2/3})O_3$: A New 1:2 Ordered Perovskite. *J. Solid State Chem.* **2003**, *170*, 198−201.

(23) Kirk, C. A.; West, A. R. Crystal Structure of the Perovskite-Related Phase of Approximate Composition $LaLi_{1/3}Ti_{2/3}O_3$. *Solid State Sci.* **2002**, *4*, 1163−1166.

(24) Hikichi, Y.; Suzuki, S. Preparation of Cubic Perovskites $A(B_{2/5}W_{3/5})O_3$ (A = Ba or Sr, B = Na or Li). *J. Am. Ceram. Soc.* **1987**, *70*, C-99−C-100.

(25) Demazeau, G.; Oh-Kim, E.; Choy, J.; Hagenmuller, P. A Vanadate (V) Oxide with Perovskite Structure: $La_2LiVO_6$, Comparison with Homologous $La_2LiMO_6$ Phases (M = Fe, Nb, Mo, Ru, Ta, Re, Os, Ir). *Mater. Res. Bull.* **1987**, *22*, 735−740.

(26) Hayashi, K.; Noguchi, H.; Ishii, M. Preparation and Vibrational Spectra of $La_2LiMO_6$ (M = Nb, Ta, Mo, Re, Ru, Os, and Ir). *Mater. Res. Bull.* **1986**, *21*, 401−406.

(27) López, M. L.; Veiga, M. L.; Rodríguez-Carvajal, J.; Fernández, F.; Jerez, A.; Pico, C. The Monoclinic Perovskite $La_2LiSbO_6$. A Rietveld Refinement of Neutron Powder Diffraction Data. *Mater. Res. Bull.* **1992**, *27*, 647−654.

(28) Wu, H.; Davies, P. K. Non-Stoichiometric 1:2 Ordered Perovskites in the $Ba(Li_{1/4}Nb_{3/4})O_3$-$Ba(Li_{2/5}W_{3/5})O_3$ System. *J. Solid State Chem.* **2004**, *177*, 3469−3478.

(29) Wu, H.; Davies, P. K. Ordered Perovskites in the $A^{2+}(Li_{1/4}Nb_{3/4})O_3$-$A^{2+}(Li_{2/5}W_{3/5})O_3$ ($A^{2+}$ = Sr, Ca) Systems. *J. Solid State Chem.* **2004**, *177*, 4305−4315.

(30) MacKenzie, K. J. D.; Smith, M. E. *Multinuclear Solid-State Nuclear Magnetic Resonance of Inorganic Materials*; Elsevier: Oxford, 2002.

(31) Ashbrook, S. E.; Smith, M. E. Solid State $^{17}$O NMR—an Introduction to the Background Principles and Applications to Inorganic Materials. *Chem. Soc. Rev.* **2006**, *35*, 718−735.

(32) Coelho, A. A. *Topas Academic*, Version 5; Coelho Software: Brisbane, Australia, 2012.

(33) Larson, A. C.; Von Dreele, R. B. *General Structure Analysis System (GSAS)*; Los Alamos National Laboratory: Los Alamos, NM, 1994.

(34) Toby, B. H. EXPGUI, a Graphical User Interface for GSAS. *J. Appl. Crystallogr.* **2001**, *34*, 210−213.

(35) Perdew, J. P.; Burke, K.; Ernzerhof, M. Generalized Gradient Approximation Made Simple. *Phys. Rev. Lett.* **1996**, *77*, 3865−3868.

(36) Kresse, G.; Furthmüller, J. Efficient Iterative Schemes for *Ab Initio* Total-Energy Calculations Using a Plane-Wave Basis Set. *Phys. Rev. B: Condens. Matter Mater. Phys.* **1996**, *54*, 11169−11186.

(37) Kresse, G.; Joubert, D. From Ultrasoft Pseudopotentials to the Projector Augmented-Wave Method. *Phys. Rev. B: Condens. Matter Mater. Phys.* **1999**, *59*, 1758−1775.

(38) Pickard, C. J.; Mauri, F. All-Electron Magnetic Response with Pseudopotentials: NMR Chemical Shifts. *Phys. Rev. B: Condens. Matter Mater. Phys.* **2001**, *63*, 245101.

(39) Yates, J. R.; Pickard, C. J.; Mauri, F. Calculation of NMR Chemical Shifts for Extended Systems Using Ultrasoft Pseudopotentials. *Phys. Rev. B: Condens. Matter Mater. Phys.* **2007**, *76*, 024401.

(40) Clark, S. J.; Segall, M. D.; Pickard, C. J.; Hasnip, P. J.; Probert, M. I. J.; Refson, K.; Payne, M. C. First Principles Methods Using CASTEP. *Z. Kristallogr. - Cryst. Mater.* **2005**, *220*, 567−570.

(41) Middlemiss, D. S.; Blanc, F.; Pickard, C. J.; Grey, C. P. Solid-State NMR Calculations for Metal Oxides and Gallates: Shielding and Quadrupolar Parameters for Perovskites and Related Phases. *J. Magn. Reson.* **2010**, *204*, 1−10.

(42) Frydman, L.; Harwood, J. S. Isotropic Spectra of Half-Integer Quadrupolar Spins from Bidimensional Magic-Angle Spinning NMR. *J. Am. Chem. Soc.* **1995**, *117*, 5367−5368.

(43) Medek, A.; Harwood, J. S.; Frydman, L. Multiple-Quantum Magic-Angle Spinning NMR: A New Method for the Study of Quadrupolar Nuclei in Solids. *J. Am. Chem. Soc.* **1995**, *117*, 12779−12787.

(44) Amoureux, J.-P.; Fernandez, C.; Steuernagel, S. Z Filtering in MQMAS NMR. *J. Magn. Reson., Ser. A* **1996**, *123*, 116−118.

(45) Lacassagne, V.; Bessada, C.; Florian, P.; Bouvet, S.; Ollivier, B.; Coutures, J.-P.; Massiot, D. Structure of High-Temperature NaF−$AlF_3$−$Al_2O_3$ Melts: A Multinuclear NMR Study. *J. Phys. Chem. B* **2002**, *106*, 1862−1868.

(46) Lacassagne, V.; Bessada, C.; Ollivier, B.; Massiot, D.; Florian, P.; Coutures, J.-P. Étude de La Transition Solide/liquide de La Cryolithe Par Résonance Magnétique Nucléaire de $^{27}$Al, $^{23}$Na et $^{19}$F. *C. R. Acad. Sci., Ser. IIb: Mec., Phys., Chim., Astron.* **1997**, *325*, 91−98.



DOI: 10.1021/acs.chemmater.6b03220
*Chem. Mater.* XXXX, XXX, XXX−XXX

(47) Bielecki, A.; Burum, D. P. Temperature Dependence of $^{207}$Pb MAS Spectra of Solid Lead Nitrate. An Accurate, Sensitive Thermometer for Variable-Temperature MAS. *J. Magn. Reson., Ser. A* **1995**, *116*, 215−220.
(48) Beckmann, P. A.; Dybowski, C. A Thermometer for Nonspinning Solid-State NMR Spectroscopy. *J. Magn. Reson.* **2000**, *146*, 379−380.
(49) Becker, K. D. Temperature Dependence of NMR Chemical Shifts in Cuprous Halides. *J. Chem. Phys.* **1978**, *68*, 3785−3793.
(50) Wu, J.; Kim, N.; Stebbins, J. F. Temperature Calibration for High-Temperature MAS NMR to 913 K: $^{63}$Cu MAS NMR of CuBr and CuI, and $^{23}$Na MAS NMR of $NaNbO_3$. *Solid State Nucl. Magn. Reson.* **2011**, *40*, 45−50.
(51) Woodward, P. M. Octahedral Tilting in Perovskites. I. Geometrical Considerations. *Acta Crystallogr., Sect. B: Struct. Sci.* **1997**, *53*, 32−43.
(52) Sommariva, M.; Catti, M. Neutron Diffraction Study of Quenched $Li_{0.3}La_{0.567}TiO_3$ Lithium Ion Conducting Perovskite. *Chem. Mater.* **2006**, *18*, 2411−2417.
(53) García-Martín, S.; Alario-Franco, M. A.; Ehrenberg, H.; Rodríguez-Carvajal, J.; Amador, U. Crystal Structure and Microstructure of Some $La_{2/3-x}Li_{3x}TiO_3$ Oxides: An Example of the Complementary Use of Electron Diffraction and Microscopy and Synchrotron X-Ray Diffraction To Study Complex Materials. *J. Am. Chem. Soc.* **2004**, *126*, 3587−3596.
(54) Ibarra, J.; Várez, A.; León, C.; Santamaría, J.; Torres-Martínez, L. M.; Sanz, J. Influence of Composition on the Structure and Conductivity of the Fast Ionic Conductors $La_{2/3-x}Li_{3x}TiO_3$ ($0.03 \le x \le 0.167$). *Solid State Ionics* **2000**, *134*, 219−228.
(55) Kennedy, B. J.; Howard, C. J.; Kubota, Y.; Kato, K. Phase Transition Behaviour in the *A*-Site Deficient Perovskite Oxide $La_{1/3}NbO_3$. *J. Solid State Chem.* **2004**, *177*, 4552−4556.
(56) Khalyavin, D. D.; Senos, A. M. R.; Mantas, P. Q. Crystal Structure of $La_4Mg_3W_3O_{18}$ Layered Oxide. *J. Phys.: Condens. Matter* **2005**, *17*, 2585−2595.
(57) Yashima, M.; Itoh, M.; Inaguma, Y.; Morii, Y. Crystal Structure and Diffusion Path in the Fast Lithium-Ion Conductor $La_{0.62}Li_{0.16}TiO_3$. *J. Am. Chem. Soc.* **2005**, *127*, 3491−3495.
(58) Fourquet, J. L.; Duroy, H.; Crosnier-Lopez, M. P. Structural and Microstructural Studies of the Series $La_{2/3-x}Li_{3x}\square_{1/3-2x}TiO_3$. *J. Solid State Chem.* **1996**, *127*, 283−294.
(59) Khalyavin, D. D.; Senos, A. M. R.; Mantas, P. Q.; Argyriou, D. N.; Gomes, I. T.; Vieira, L. G.; Ribeiro, J. L. Structure and Dielectric Characterization of a New *A*-Site Deficient $La_{5/3}MgTaO_6$ Perovskite. *J. Solid State Chem.* **2007**, *180*, 41−48.
(60) Grau-Crespo, R.; Hamad, S.; Catlow, C. R. A.; de Leeuw, N. H. Symmetry-Adapted Configurational Modelling of Fractional Site Occupancy in Solids. *J. Phys.: Condens. Matter* **2007**, *19*, 256201.
(61) Khalyavin, D. D.; Lopes, A. B.; Senos, A. M. R.; Mantas, P. Q. Crystal Structure of $La_6Mg_4Ta_2W_2O_{24}$ Oxide: A Representative of a Novel $A_{3n}B'_{2n}B''_{2n}O_{12n}$ Homologous Series with $n = 2$. *Chem. Mater.* **2006**, *18*, 3843−3849.
(62) Xu, Z.; Stebbins, J. F. Cation Dynamics and Diffusion in Lithium Orthosilicate: Two-Dimensional Lithium-6 NMR. *Science* **1995**, *270*, 1332−1334.
(63) Xu, Z.; Stebbins, J. F. $^{6}$Li Nuclear Magnetic Resonance Chemical Shifts, Coordination Number and Relaxation in Crystalline and Glassy Silicates. *Solid State Nucl. Magn. Reson.* **1995**, *5*, 103−112.
(64) Wilkening, M.; Küchler, W.; Heitjans, P. From Ultraslow to Fast Lithium Diffusion in the 2D Ion Conductor $Li_{0.7}TiS_2$ Probed Directly by Stimulated-Echo NMR and Nuclear Magnetic Relaxation. *Phys. Rev. Lett.* **2006**, *97*, 065901.
(65) Kuhn, A.; Sreeraj, P.; Pöttgen, R.; Wiemhöfer, H. D.; Wilkening, M.; Heitjans, P. Li Ion Diffusion in the Anode Material $Li_{12}Si_7$: Ultrafast Quasi-1D Diffusion and Two Distinct Fast 3D Jump Processes Separately Revealed by $^{7}$Li NMR Relaxometry. *J. Am. Chem. Soc.* **2011**, *133*, 11018−11021.
(66) Buschmann, H.; Dölle, J.; Berendts, S.; Kuhn, A.; Bottke, P.; Wilkening, M.; Heitjans, P.; Senyshyn, A.; Ehrenberg, H.; Lotnyk, A.; Duppel, V.; Kienle, L.; Janek, J. Structure and Dynamics of the Fast Lithium Ion Conductor "$Li_7La_3Zr_2O_{12}$. *Phys. Chem. Chem. Phys.* **2011**, *13*, 19378−19392.
(67) Blanc, F.; Middlemiss, D. S.; Gan, Z.; Grey, C. P. Defects in Doped $LaGaO_3$ Anionic Conductors: Linking NMR Spectral Features, Local Environments, and Defect Thermodynamics. *J. Am. Chem. Soc.* **2011**, *133*, 17662−17672.
(68) Epp, V.; Gün, O.; Deiseroth, H.-J.; Wilkening, M. Long-Range $Li^+$ Dynamics in the Lithium Argyrodite $Li_7PSe_6$ as Probed by Rotating-Frame Spin-Lattice Relaxation NMR. *Phys. Chem. Chem. Phys.* **2013**, *15*, 7123−7132.
(69) Enciso-Maldonado, L.; Dyer, M. S.; Jones, M. D.; Li, M.; Payne, J. L.; Pitcher, M. J.; Omir, M. K.; Claridge, J. B.; Blanc, F.; Rosseinsky, M. J. Computational Identification and Experimental Realization of Lithium Vacancy Introduction into the Olivine $LiMgPO_4$. *Chem. Mater.* **2015**, *27*, 2074−2091.
(70) Liu, T.; Leskes, M.; Yu, W.; Moore, A. J.; Zhou, L.; Bayley, P. M.; Kim, G.; Grey, C. P. Cycling Li-$O_2$ Batteries via LiOH Formation and Decomposition. *Science* **2015**, *350*, 530−533.
(71) Bonhomme, C.; Gervais, C.; Babonneau, F.; Coelho, C.; Pourpoint, F.; Azaïs, T.; Ashbrook, S. E.; Griffin, J. M.; Yates, J. R.; Mauri, F.; Pickard, C. J. First-Principles Calculation of NMR Parameters Using the Gauge Including Projector Augmented Wave Method: A Chemist's Point of View. *Chem. Rev.* **2012**, *112*, 5733−5779.
(72) Smith, M. E.; van Eck, E. R. H. Recent Advances in Experimental Solid State NMR Methodology for Half-Integer Spin Quadrupolar Nuclei. *Prog. Nucl. Magn. Reson. Spectrosc.* **1999**, *34*, 159−201.
(73) Ashbrook, S. E.; Dawson, D. M. Exploiting Periodic First-Principles Calculations in NMR Spectroscopy of Disordered Solids. *Acc. Chem. Res.* **2013**, *46*, 1964−1974.
(74) Shannon, R. D. Revised Effective Ionic Radii and Systematic Studies of Interatomic Distances in Halides and Chalcogenides. *Acta Crystallogr., Sect. A: Cryst. Phys., Diffr., Theor. Gen. Crystallogr.* **1976**, *32*, 751−767.
(75) Böhmer, R.; Jeffrey, K. R.; Vogel, M. Solid-State Li NMR with Applications to the Translational Dynamics in Ion Conductors. *Prog. Nucl. Magn. Reson. Spectrosc.* **2007**, *50*, 87−174.
(76) Emery, J.; Buzare, J. Y.; Bohnke, O.; Fourquet, J. L. Lithium-7 NMR and Ionic Conductivity Studies of Lanthanum Lithium Titanate Electrolytes. *Solid State Ionics* **1997**, *99*, 41−51.
(77) Bucheli, W.; Arbi, K.; Sanz, J.; Nuzhnyy, D.; Kamba, S.; Várez, A.; Jimenez, R. Near Constant Loss Regime in Fast Ionic Conductors Analyzed by Impedance and NMR Spectroscopies. *Phys. Chem. Chem. Phys.* **2014**, *16*, 15346−15354.
(78) Abragam, A. *The Principles of Nuclear Magnetism*; Oxford University Press: Oxford, 1961.
(79) Heitjans, P.; Schirmer, A.; Indris, S. *NMR and β-NMR Studies of Diffusion in Interface-Dominated and Disordered Solids*; Heitjans, P., Kärger, J., Eds.; Springer-Verlag: Berlin, 2005.
(80) Wilkening, M.; Heitjans, P. From Micro to Macro: Access to Long-Range $Li^+$ Diffusion Parameters in Solids via Microscopic $^{6,7}$Li Spin-Alignment Echo NMR Spectroscopy. *ChemPhysChem* **2012**, *13*, 53−65.
(81) Bloembergen, N.; Purcell, E. M.; Pound, R. V. Relaxation Effects in Nuclear Magnetic Resonance Absorption. *Phys. Rev.* **1948**, *73*, 679−712.
(82) Irvine, J. T. S.; Sinclair, D. C.; West, A. R. Electroceramics: Characterization by Impedance Spectroscopy. *Adv. Mater.* **1990**, *2*, 132−138.
(83) Stramare, S.; Thangadurai, V.; Weppner, W. Lithium Lanthanum Titanates: A Review. *Chem. Mater.* **2003**, *15*, 3974−3990.
(84) García-Martín, S.; Amador, U.; Morata-Orrantia, A.; Rodríguez-Carvajal, J.; Alario-Franco, M. Á. Structure, Microstructure, Composition and Properties of Lanthanum Lithium Titanates and Some Substituted Analogues. *Z. Anorg. Allg. Chem.* **2009**, *635*, 2363−2373.



DOI: 10.1021/acs.chemmater.6b03220
*Chem. Mater.* XXXX, XXX, XXX−XXX

(85) Marezio, M.; Remeika, J. P.; Dernier, P. D. The Crystal Chemistry of the Rare Earth Orthoferrites. *Acta Crystallogr., Sect. B: Struct. Crystallogr. Cryst. Chem.* **1970**, *26*, 2008−2022.

(86) López, M. L.; Veiga, M. L.; Jerez, A.; Pico, C. Synthesis and Crystal Structure of $La_2LiSbO_6$. *Mater. Res. Bull.* **1990**, *25*, 1271−1277.

(87) Catti, M.; Sommariva, M.; Ibberson, R. M. Tetragonal Superstructure and Thermal History of $Li_{0.3}La_{0.567}TiO_3$ (LLTO) Solid Electrolyte by Neutron Diffraction. *J. Mater. Chem.* **2007**, *17*, 1300−1307.

(88) Alonso, J. A.; Sanz, J.; Santamaría, J.; León, C.; Várez, A.; Fernández-Díaz, M. T. On the Location of $Li^+$ Cations in the Fast Li-Cation Conductor $La_{0.5}Li_{0.5}TiO_3$ Perovskite. *Angew. Chem., Int. Ed.* **2000**, *39*, 619−621.

(89) Momma, K.; Izumi, F. *VESTA 3* for Three-Dimensional Visualization of Crystal, Volumetric and Morphology Data. *J. Appl. Crystallogr.* **2011**, *44*, 1272−1276.

(90) Baur, W. H. The Geometry of Polyhedral Distortions. Predictive Relationships for the Phosphate Group. *Acta Crystallogr., Sect. B: Struct. Crystallogr. Cryst. Chem.* **1974**, *30*, 1195−1215.

(91) Robinson, K.; Gibbs, G. V.; Ribbe, P. H. Quadratic Elongation: A Quantitative Measure of Distortion in Coordination Polyhedra. *Science* **1971**, *172*, 567−570.

(92) Buttner, R. H.; Maslen, E. N. Electron Difference Density and Structural Parameters in $CaTiO_3$. *Acta Crystallogr., Sect. B: Struct. Sci.* **1992**, *48*, 644−649.

(93) Inaguma, Y. Fast Percolative Diffusion in Lithium Ion-Conducting Perovskite-Type Oxides. *J. Ceram. Soc. Japan* **2006**, *114*, 1103−1110.

(94) Rivera, A.; Sanz, J. Lithium Dynamics in the Fast Ionic Conductor $Li_{0.18}La_{0.61}TiO_3$ Probed by $^7Li$ NMR Spectroscopy. *Phys. Rev. B: Condens. Matter Mater. Phys.* **2004**, *70*, 94301.

(95) Rivera, A.; León, C.; Santamaría, J.; Varez, A.; Paris, M. A.; Sanz, J. $Li_{3x}La_{(2/3)-x}TiO_3$ Fast Ionic Conductors. Correlation between Lithium Mobility and Structure. *J. Non-Cryst. Solids* **2002**, *307−310*, 992−998.

(96) Catti, M. Short-Range Order and $Li^+$ Ion Diffusion Mechanisms in $\mathbf{Li_5La_9\square_2(TiO_3)_{16}}$ (LLTO). *Solid State Ionics* **2011**, *183*, 1−6.

(97) Jalem, R.; Yamamoto, Y.; Shiiba, H.; Nakayama, M.; Munakata, H.; Kasuga, T.; Kanamura, K. Concerted Migration Mechanism in the Li Ion Dynamics of Garnet-Type $Li_7La_3Zr_2O_{12}$. *Chem. Mater.* **2013**, *25*, 425−430.

(98) Lang, B.; Ziebarth, B.; Elsässer, C. Lithium Ion Conduction in $LiTi_2(PO_4)_3$ and Related Compounds Based on the NASICON Structure: A First-Principles Study. *Chem. Mater.* **2015**, *27*, 5040−5048.

(99) Kuhn, A.; Duppel, V.; Lotsch, B. V. Tetragonal $Li_{10}GeP_2S_{12}$ and $Li_7GePS_8$ − Exploring the Li Ion Dynamics in LGPS Li Electrolytes. *Energy Environ. Sci.* **2013**, *6*, 3548−3552.

(100) Epp, V.; Gün, Ö.; Deiseroth, H.-J.; Wilkening, M. Highly Mobile Ions: Low Temperature NMR Directly Probes Extremely Fast $Li^+$ Hopping in Argyrodite-Type $Li_6PS_5Br$. *J. Phys. Chem. Lett.* **2013**, *4*, 2118−2123.

(101) Epp, V.; Ma, Q.; Hammer, E.; Tietz, F.; Wilkening, M. Very Fast Bulk Li Ion Diffusivity in Crystalline $Li_{1.5}Al_{0.5}Ti_{1.5}(PO_4)_3$ as Seen by NMR Relaxometry. *Phys. Chem. Chem. Phys.* **2015**, *17*, 32115−32121.

(102) Huberman, B. A.; Boyce, J. B. Breakdown of Absolute Rate Theory and Prefactor Anomalies in Superionic Conductors. *Solid State Commun.* **1978**, *25*, 843−846.

(103) Latie, L.; Villeneuve, G.; Conte, D.; Le Flem, G. Ionic Conductivity of Oxides with General Formula $Li_xLn_{1/3}Nb_{1-x}Ti_xO_3$ (*Ln* = La, Nd). *J. Solid State Chem.* **1984**, *51*, 293−299.

(104) Deng, Y.; Eames, C.; Chotard, J.-N.; Lalère, F.; Seznec, V.; Emge, S.; Pecher, O.; Grey, C. P.; Masquelier, C.; Islam, M. S. Structural and Mechanistic Insights into Fast Lithium-Ion Conduction in $Li_4SiO_4$-$Li_3PO_4$ Solid Electrolytes. *J. Am. Chem. Soc.* **2015**, *137*, 9136−9145.

(105) Arbi, K.; Lazarraga, M. G.; Ben Hassen Chehimi, D.; Ayadi-Trabelsi, M.; Rojo, J. M.; Sanz, J. Lithium Mobility in LiTiR(PO) Compounds (R = Al,Ga,Sc,In) as Followed by NMR and Impedance Spectroscopy. *Chem. Mater.* **2004**, *16*, 255−262.

(106) León, C.; Lucia, M.; Santamaria, J.; París, M.; Sanz, J.; Várez, A. Electrical Conductivity Relaxation and Nuclear Magnetic Resonance of Li Conducting $Li_{0.5}La_{0.5}TiO_3$. *Phys. Rev. B: Condens. Matter Mater. Phys.* **1996**, *54*, 184−189.

(107) Kim, N.; Hsieh, C. H.; Huang, H.; Prinz, F. B.; Stebbins, J. F. High Temperature $^{17}O$ MAS NMR Study of Calcia, Magnesia, Scandia and Yttria Stabilized Zirconia. *Solid State Ionics* **2007**, *178*, 1499−1506.

(108) Bottke, P.; Freude, D.; Wilkening, M. Ultraslow Li Exchange Processes in Diamagnetic $Li_2ZrO_3$ as Monitored by EXSY NMR. *J. Phys. Chem. C* **2013**, *117*, 8114−8119.

(109) Holmes, L.; Peng, L.; Heinmaa, I.; O'Dell, L. A.; Smith, M. E.; Vannier, R.-N.; Grey, C. P. Variable-Temperature $^{17}O$ NMR Study of Oxygen Motion in the Anionic Conductor $Bi_{26}Mo_{10}O_{69}$. *Chem. Mater.* **2008**, *20*, 3638−3648.




DOI: 10.1021/acs.chemmater.6b03220
*Chem. Mater.* XXXX, XXX, XXX−XXX